The 3D Crustal Structure of the Wilkes Subglacial Basin, East Antarctica, Using Variation of Information Joint Inversion of Gravity and Magnetic Data

Maximilian Lowe[1,2] [ID]**, Tom Jordan[1]** [ID]**, Max Moorkamp[3,4]** [ID]**, Jörg Ebbing[5]** [ID]**, Chris Green[6]** [ID]**, Mareen Lösing[7,8]** [ID]**, Teal Riley[1]** [ID]**, and Robert Larter[1]** [ID]

[1]NERC British Antarctic Survey, Cambridge, UK, [2]School of Geosciences, University of Edinburgh, Edinburgh, UK, [3]Department of Earth and Environmental Sciences, Ludwig Maximilian University of Munich, Munich, Germany, [4]Now at: Institute of Applied Geosciences, Technical University Berlin, Berlin, Germany, [5]Institute of Geosciences, Kiel University, Kiel, Germany, [6]School of Earth and Environment, University of Leeds, Leeds, UK, [7]School of Earth Sciences, University of Western Australia, Perth, WA, Australia, [8]Australian Centre for Excellence in Antarctic Science, University of Western Australia, Perth, WA, Australia

Abstract Direct geological information in Antarctica is limited to ice free regions along the coast, high mountain ranges, or isolated nunataks. Therefore, indirect methods are required to reveal subglacial geology and heterogeneities in crustal properties, which are critical steps toward interpreting geological history. We present a 3D crustal model of density and susceptibility distribution in the Wilkes Subglacial Basin (WSB) and the Transantarctic Mountains (TAM) based on joint inversion of airborne gravity and magnetic data. The applied "variation of information" technique enforces a coupling between inferred susceptibility and density, relating these quantities to the same gravity and magnetic sources to give an enhanced inversion result. Our model reveals a large body located in the interior of the WSB interpreted as a batholithic intrusive structure, as well as a linear dense body at the margin of the Terre Adélie Craton. Density and susceptibility relationships are used to inform the interpretation of petrophysical properties and the reconstruction of the origin of those crustal bodies. The petrophysical relationship indicates that the postulated batholitic intrusion is granitic, but independent from the Granite Harbor Igneous Complex described previously in the TAM area. Emplacement of a large volume of intrusive granites can potentially elevate local geothermal heat flow significantly. Finally, we present a new conceptual tectonic model based on the inversion results, which includes development of a passive continental margin with seaward dipping basalt horizons and magmatic underplating followed by two distinct intrusive events associated with the protracted Ross Orogen.

Plain Language Summary Most rocks in Antarctica are hidden beneath a thick ice sheet. Therefore, indirect techniques are required to reveal rock provinces within Earth's crust below the ice. Rocks simultaneously influence the gravity and magnetic fields through their physical properties (density and susceptibility). Here we use both the gravity and magnetic fields to reveal rock provinces beneath the ice and use the relationship between density and susceptibility of the rocks to interpret the distribution of granitic rocks of the Transantarctic Mountains and the Wilkes Subglacial Basin region in East Antarctica. Granitic rocks can lead to elevated heat flow due to radiogenic decay of minerals within the rock and thus influence the overlying ice sheet. Based on our subsurface model of rock provinces we speculate on the tectonic evolution of the region.

1. Introduction

The Wilkes Subglacial Basin (WSB) lies between the Transantarctic Mountains (TAM) and the Terre Adélie Craton (Figure 1) and was first identified by radar data in the 1970s (Drewry, 1976). The WSB stretches ∼1,600 km from the George V Coast toward the South Pole, while its width decreases from ∼600 km close to the George V coast (Ferraccioli, Armadillo, Zunino, et al., 2009) to < 100 km toward the South Pole (Studinger et al., 2004). The subglacial geology in the WSB and TAM region is largely hidden beneath a 2–3 km thick ice sheet. Understanding the subglacial geology and crustal properties is crucial to constrain the influence of the solid Earth on the stability of the overlying ice sheet.

The WSB forms one of the largest areas of bed topography below sea level in East Antarctica, potentially reaching depths of more than 2 km below sea level in the deeply incised sub-basins (Morlighem et al., 2020) (Figure 1).

Validation: Maximilian Lowe,
Tom Jordan, Max Moorkamp,
Jörg Ebbing, Chris Green, Robert Larter
Visualization: Maximilian Lowe,
Tom Jordan
Writing – original draft:
Maximilian Lowe
Writing – review & editing: Tom Jordan,
Max Moorkamp, Jörg Ebbing,
Chris Green, Mareen Lösing, Teal Riley,
Robert Larter

Such sub-sea level basins pose a potentially high, but poorly understood, risk for the stability of the East Antarctic Ice Sheet (EAIS) and, therefore, for future sea-level rise, as they are more vulnerable to melting by warm ocean water inflow. Such melting could potentially trigger mechanisms of unstable retreat (Pollard et al., 2015; Schoof, 2007). Recent studies suggest a significant long-term contribution from the WSB region to sea-level rise within the next two centuries accompanied by major retreat of the ice sheet in the WSB region by the year 2500 (DeConto & Pollard, 2016; Stokes et al., 2022).

For the WSB itself, competing models for its evolution have been proposed since its discovery including a rift basin (Steed, 1983), extended terrane (Ferraccioli et al., 2001), as a basin adjacent to the remnants of a collapsed plateau (Bialas et al., 2007), or as a flexural down-warp of cratonic lithosphere as a consequence of the TAM uplift (Stern & ten Brink, 1989; ten Brink et al., 1997). However, the modern landscape formation of the WSB is generally believed to result from a combination of lithospheric flexure associated with the TAM uplift combined with glacial erosion (Ferraccioli, Armadillo, Jordan, et al., 2009; Jordan et al., 2013; Paxman et al., 2018, 2019).

The geology of the WSB remains disputed as the occurrence of direct geological samples is limited to ice free regions along the coast, or isolated nunataks, while the origin of geological material transported to the coast by glaciers is often ambiguous. Adjacent to the Mertz shear zone (Figure 1), on the side of the Terre Adélie Craton, ≥2,440 Ma paragneiss and granitoids are exposed, while on the WSB side of the Mertz shear zone ca. 500 Ma granites have been mapped (Finn et al., 1999). Aeromagnetic measurements in the WSB have been used to infer the presence of Beacon Supergroup sedimentary strata intruded by rocks of the Ferrar Large Igneous Province (Ferraccioli, Armadillo, Jordan, et al., 2009). Geological interpretations of the interior of the WSB are mainly derived from radar, gravity, and magnetic airborne measurements (e.g., Jordan et al., 2013).

A prominent positive magnetic anomaly exists in the central WSB, the origin of which is hypothesized to be either an intrusive arc associated with subduction (Ferraccioli, Armadillo, Jordan, et al., 2009), or associated with thinned crust attributed to continental rifting (Ferraccioli et al., 2001). Another prominent feature is a positive linear gravity anomaly associated with the craton margin (CM), which was interpreted as up-thrusted crustal material along the craton flank (Studinger et al., 2004) (Figures 2a and 2b).

The adjacent TAM, a large non-contractional mountain range, separate the warmer lithosphere of the Cretaceous-Cenozoic West Antarctic rift system and the colder and older provinces of East Antarctica (Morelli & Danesi, 2004; Robinson & Splettstoesser, 1986; ten Brink & Stern, 1992). Direct geological information is richer in the TAM compared to WSB since more rock outcrops are present in the high mountain range.

The Neoproterozoic to early Paleozoic Ross Orogen in Antarctica forms part of an active Gondwana-margin convergent plate boundary stretching from present-day eastern Australia to South America, but it is largely obscured by ice and younger sedimentary cover. Ross Orogeny magmatism developed over a period of ca. 100 Myr (ca. 600–500 Ma; (Goodge et al., 2024)), associated with multiple magmatic peaks (Paulsen et al., 2023), including the Cambro-Ordovician Granite Harbor intrusive complex. In Northern Victoria Land, adjacent to our study area, the Ross Orogen is dominated by five geological terranes and units identified in the TAM; they are from grid-west (geographic east) to grid-east (geographic west) the Robertson Bay Terrane, the Millen Schist, the Bowers Terrane, the Wilson Terrane, and Granite Harbor Igneous Complex (Figures 1a and 1b). These terranes are all intruded by doleritic sills of the Early Jurassic Ferrar large igneous province, and in places overlain by the associated Kirkpatrick basaltic lavas (Estrada et al., 2016 and references therein). Detrital zircon analysis from sedimentary rocks shows a decrease in likely depositional age from the Wilson Terrane toward grid-west to the Robertson Bay group from >550 Ma to <550 Ma, (Estrada et al., 2016). The emplacement of the Granite Harbor Igneous Complex corresponds to the younger ages seen in the detrital zircon populations (Estrada et al., 2016), while the source for the older (>550 Ma) material remains speculative.

Radiogenic heat production is predicted to contribute up to 40% to the surface Geothermal heat flow (GHF) (Artemieva & Mooney, 2001; Haeger et al., 2022; Hasterok & Chapman, 2011). However, due to the lack of information on subglacial geology and crustal properties, incorporating accurate thermal crustal parameters, such as radiogenic heat production and thermal conductivity, is challenging. Therefore, current geophysically derived GHF models commonly use global average values instead (Haeger et al., 2022; Lösing & Ebbing, 2021b; Lowe, Mather, et al., 2023; Martos et al., 2017, 2017b; Shen et al., 2020; Stål et al., 2021). For more in depth discussion of current Antarctic GHF models the reader is referred to (Burton-Johnson et al., 2020; Reading et al., 2022).
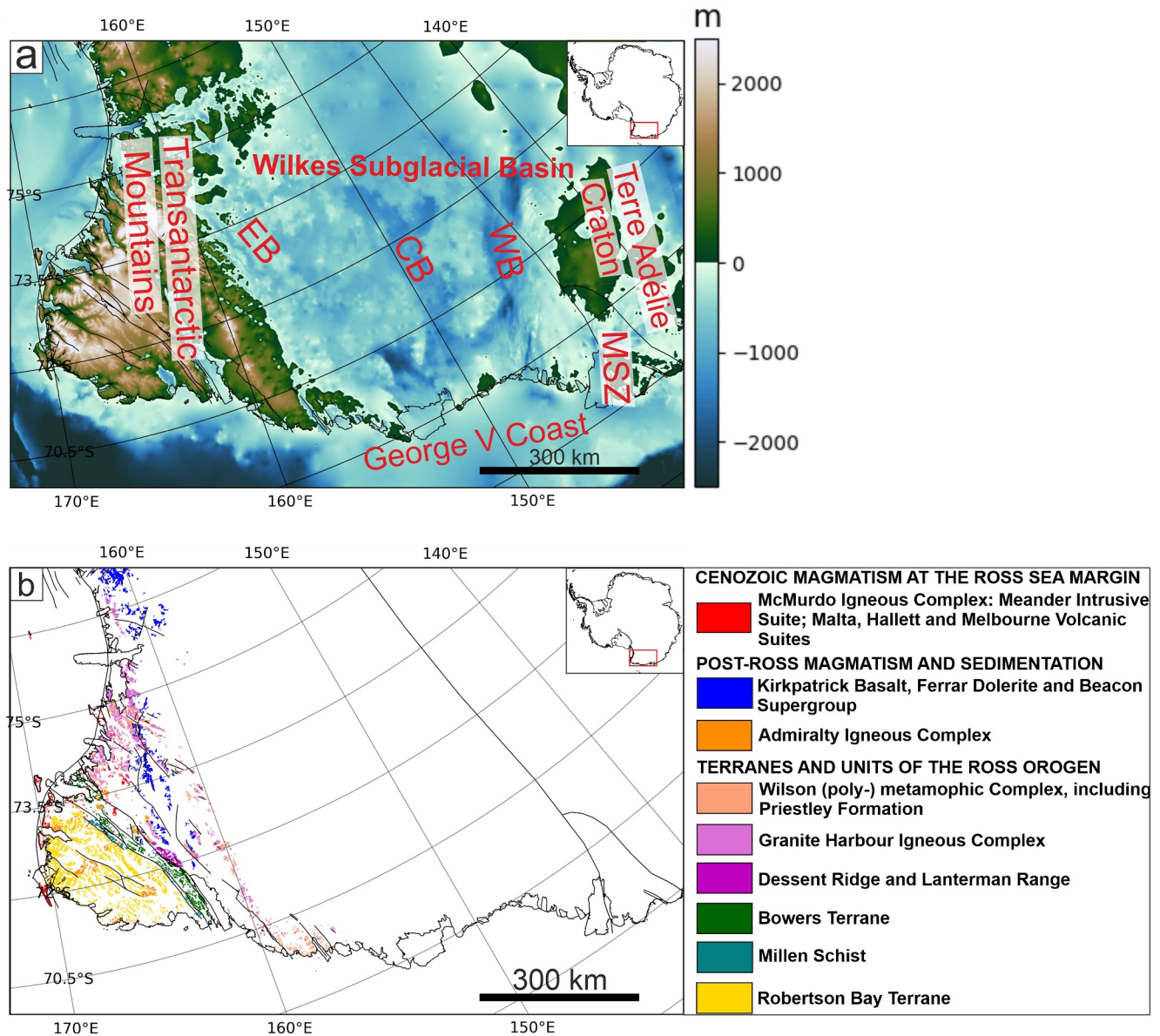
Figure 1. (a) Bedrock topography of the Transantarctic Mountains and Wilkes Subglacial Basin from the Bedmachine model version 3 (Morlighem et al., 2020). EB: Eastern Basin; CB: Central Basin; WB: Western Basin; MSZ: Mertz shear zone. Black lines mark ice grounding lines and ice shelf extents from the Scientific Committee on Antarctic Research Antarctic Digital Database. Black lines in the interior of nVL indicate faults based on (Cox et al., 2023a, 2023b). (b) Tectonic provinces. Geological information taken from (Cox et al., 2023a), classification adapted from (Estrada et al., 2016).

The objectives of this study are to identify crustal structures, crustal geological provinces and intrusive bodies, constrain their dimensions in 3D, and also to identify the Terre Adélie Craton boundary. For this purpose, we conduct a joint inversion of gravity and magnetic data to obtain petrologically realistic parameter distributions, specifically of density and susceptibility. The geophysical inversion uses the joint inversion framework JIF3D (Moorkamp et al., 2011), which implements the Variation of Information (VI) technique to introduce a coupling between the inverted density and susceptibility sources (Lösing et al., 2022; Moorkamp, 2021, 2022). Subsequently, the obtained density and susceptibility relationship of the inversion model is used to identify crustal rock provinces and infer potential rock types. The geophysical and petrophysical interpretation of the inversion results is the basis for our tectonic evolution model. Although geophysical mapping can give an indication of tectonic boundaries and 2D models of gravity or magnetic data alone give some insights into the source bodies, the 3D architecture and properties of the crust are required to more fully understand the origins and implications of this
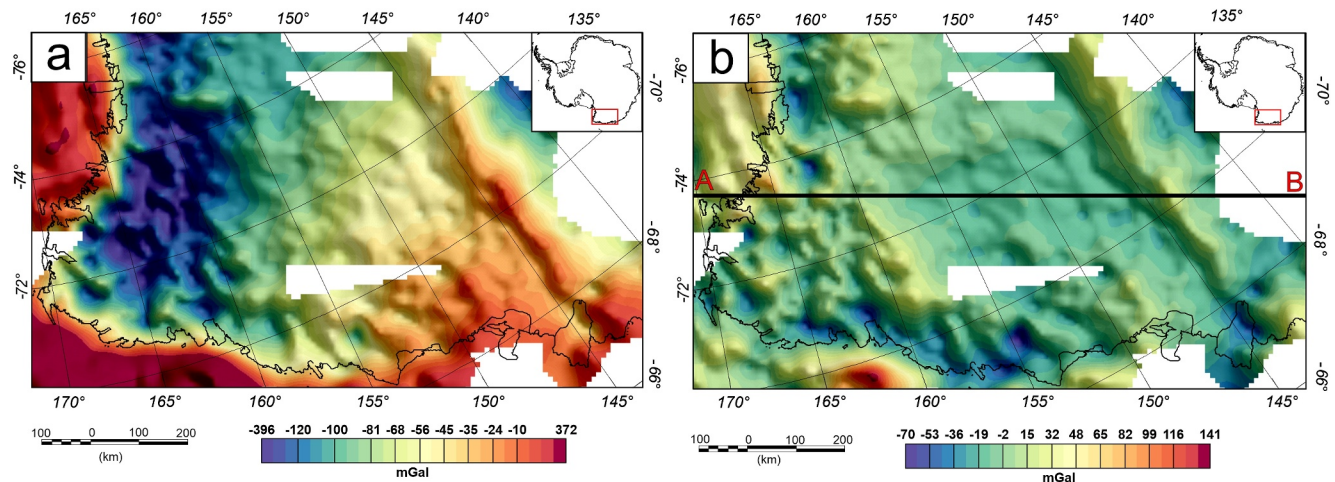
Figure 2. (a) Bouguer Anomaly compilation including AntGG data (Scheinert et al., 2016b) and regional gravity data (Reitmayr et al., 2003; Zanutta et al., 2018). (b) Residual gravity map obtained by subtracting the gravity response from the lithospheric model of (Pappa, Ebbing, Ferraccioli, et al., 2019) and then subtracting the mean value of the residual field. Both gravity grids have a grid spacing of 10 km. Black line indicates location of cross section profile in Figure 8.

key basin. Models of gravity or magnetic data are non-unique and can be hard to interpret in terms of petro-physical properties We therefore turn to joint inversion of gravity and magnetic data to provide this information as joint inversion acts to minimize the parameter space considered, producing a sharper and better constrained geophysical output.

2. Data

This section describes the geophysical data and the boundary conditions used to obtain a joint inversion model for 3D crustal density and susceptibility distribution.

2.1. Gravity Data

Bouguer gravity anomaly data (Figure 2a), are taken from AntGG (Scheinert et al., 2016a). The Bouguer anomaly was calculated using a spherical prism approach with an integration radius of 300 km using standard densities of 2,670 kg/m^3 for rock, 917 kg/m^3 for ice and 1,025 kg/m^3 for water (Scheinert et al., 2016b). Where applied, the Bouguer correction removes the signatures of surface and subglacial topography, as well as the gravity signature associated with the observed ice sheet and ocean basins. The AntGG gravity compilation includes airborne, terrestrial, and shipborne measurements, which are provided, after integration and correction, as a grid of points with a spacing of 10 km. Data gaps in AntGG are filled in with Bouguer gravity anomaly data from the Ganovex VII—ItaliAntartide XV survey (Reitmayr et al., 2003) and recent ground measurements conducted within the Italian National Program for Antarctic Research activities (Zanutta et al., 2018) (Figure S1 in Supporting Information S1). This data compilation, including AntGG and additional ground data points, is re-gridded with a spacing of 10 km and a blanking distance of 40 km using the minimum curvature gridding function in Oasis Montaj (Seequent; Reading, England) (W H F Smith & Wessel, 1990) to produce the Bouguer anomaly grid of the WSB and TAM region. The blanking distance is the maximum distance from a valid point where values will be interpolated. Beyond this distance dummy (NaNs) values are returned. The Bouguer anomaly grid is subsequently upward continued to a constant observation height of 10 km above the geoid (Figure 2a) using the Compudrape algorithm in Oasis Montaj (Cordell, 1985). This method takes data collected at various levels and generates a series of data slices using standard fixed distance Fast Fourier Transformation continuation method (Blakely, 1996). The new field, continued to a uniform level, is interpolated from the suite of data slices.

The Bouguer anomaly map shows a large negative signal in the TAM region, where a crustal root is present beneath the mountain range (Baranov et al., 2021; Block et al., 2009; Hansen et al., 2016; Pappa, Ebbing, & Ferraccioli, 2019). A prominent positive linear feature exists in the Bouguer anomaly map following the grid-east edge of the WSB and might indicate the transition zone at the margin of the Terre Adélie Craton (Goodge &
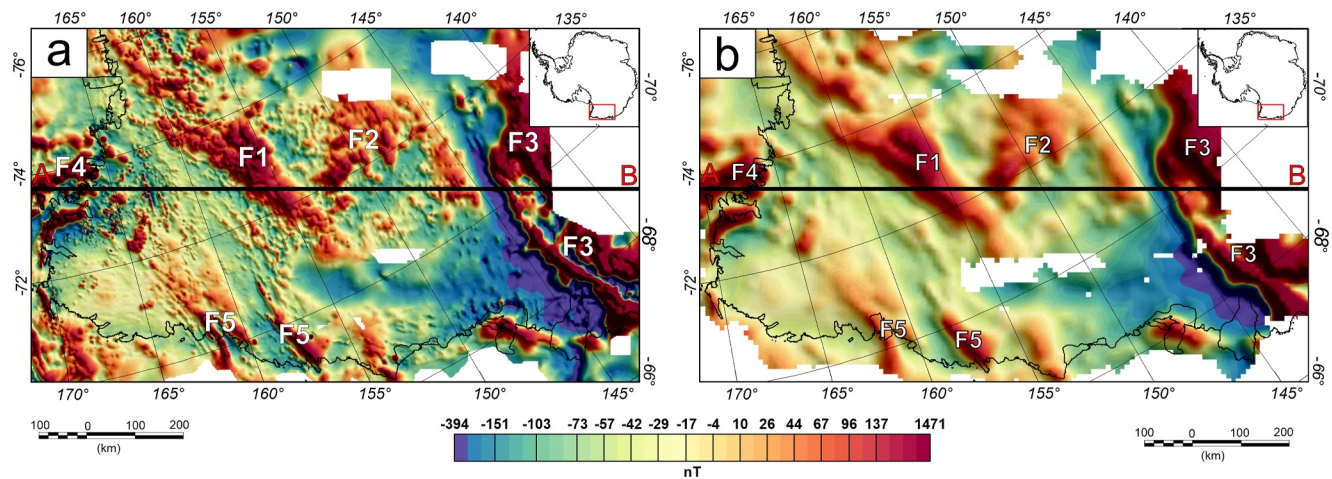
Figure 3. (a) Magnetic anomaly grid from ADMAP-2 (Golynsky et al., 2018b) with a grid spacing of 1.5 km. (b) Regridded ADMAP-2 magnetic data with a grid spacing of 10 km and upward continued at a constant height of 10 km to match the resolution and upward-continued height of the gravity compilation. Black line indicates location of cross section profile in Figure 8. Features F1–F5 relate to magnetic anomalies discussed in the main text.

Finn, 2010). To remove the gravity contribution below the Moho interface the vertical gravity response from the Antarctic continent-wide forward lithospheric model from (Pappa, Ebbing, Ferraccioli, et al., 2019) was subtracted (Figure S2 in Supporting Information S1). This model contains a homogeneous crust, were density only increases with depth due to the increasing pressure and a variable mantle. By subtracting this model, we corrected for a variable mantle and Moho depth variation and, therefore, the resulting residuals correspond to variations within the crust. The lithospheric model is presented at 10 km observation height and is the reason all input data are upward continued to this constant height. In the resulting residual gravity map (Figure S2 in Supporting Information S1) the large negative signal beneath the TAM is absent, while the relative positive linear crustal structure is preserved. Furthermore, the mean value (92.5 mGal) of the residual gravity field is removed to shift the residual gravity field to a mean level of 0 mGal (Figure 2b).

2.2. Magnetic Data

3.5 million line-km of aeromagnetic and marine magnetic measurements in Antarctica and the Southern Ocean are included in the ADMAP-2 magnetic data compilation (Golynsky et al., 2018b). The gridded ADMAP-2 product (Figure 3a) has a grid spacing of 1.5 km. Applied data processing and corrections of the magnetic data include subtraction of the International Geomagnetic Reference Field, diurnal effects correction, high-frequency error correction, leveling, regional gridding, and merging of regional grids into a continent-wide compilation (Golynsky et al., 2018b). For the inversion, the magnetic line data from the ADMAP-2 compilation are gridded with a grid spacing of 10 km to match the grid spacing of the gravity data (Section 3.1). Again, the gridding was performed using the minimum curvature gridding function with a blanking distance of 10 km in Oasis Montaj. The magnetic grid is also upward continued to a height of 10 km (Figure 3b) to be consistent with the gravity data using again the Compudrape function within Oasis Montaj. The upward continuation of the magnetic data functions as a lowpass filter, removing high frequency content, while broad magnetic anomalies are preserved. The upward continuation of the magnetic data attenuates the short wavelengths. The minimum wavelength of the upward continued data is approximately 20 km.

The magnetic anomaly grid shows a broad linear feature oriented grid-northwest—grid-southeast (Figure 3, F1) in the central part of the WSB, the origin of which has been hypothesized to be a failed rift or an arc-related intrusive body (Ferraccioli & Bozzo, 2003; Ferraccioli, Armadillo, Zunino, et al., 2009). Perpendicular to this feature a positive magnetic anomaly is visible (F2). A strong linear anomaly exists grid-east to the WSB toward the CM (F3), where the magnetic anomaly rapidly increases to values of ~1,500 nT compared to the dominating ± 300 nT range in the WSB and TAM area. Smaller magnetic anomalies are observed offshore to the grid-west (F4) and along the Rennick Graben and Matusevich glacier region (F5).
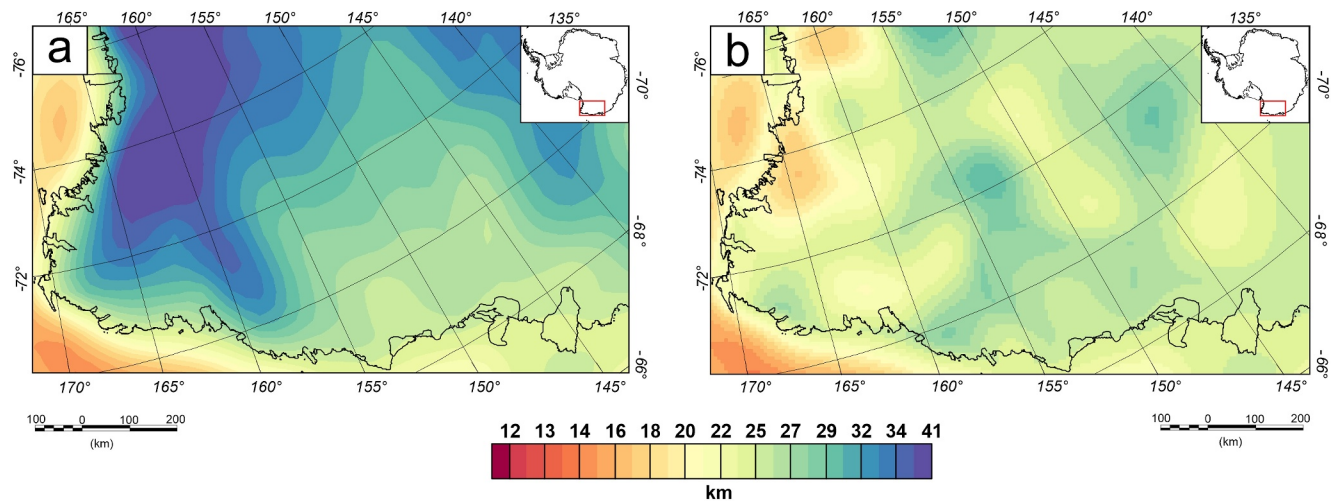
Figure 4. (a) Moho depth map derived from Satellite gravity measurements (Pappa, Ebbing, & Ferraccioli, 2019). (b) Curie point depths estimated (Lowe, Mather, et al., 2023) based on kriging interpolation, clipped to be shallower than the Moho.

2.3. Uncertainty of Airborne Data

The uncertainty of airborne gravity and magnetic measurements depends on several factors such as the sensor, the processing or turbulence during the measurement campaign. The input data are a compilation of multiple surveys with varying data uncertainty. The gravity survey WISE-ISODYN, which is the dominant survey in the data compilation has a reported uncertainty of 2.8 mGal (Jordan et al., 2013). Error estimation of airborne magnetic data is assessed by crossovers of flight lines. However, crossovers are used to level the survey itself, which eventually leads to a 0 nT offset at the crossovers. A conservative uncertainty estimation of the airborne magnetic data is in the order of 5–15 nT.

2.4. Moho Depth and Curie Depth

Moho depth estimates (Figure 4a) are taken from satellite gravity inversion (Pappa, Ebbing, & Ferraccioli, 2019). The Moho interface is used as the bottom boundary condition for the density inversion.

Curie Point Depth (CPD) estimates are taken from (Lowe, Mather, et al., 2023) and used as a bottom boundary condition for the susceptibility inversion. Below the CPD, often associated with the 580°C isotherm, ferrimagnetic materials lose their ability to maintain a preferential orientation in the direction of the inducing, main field. Therefore, the joint inversion of magnetic and gravity data needs to be limited to crustal depth above the CPD. The CPD estimates from (Lowe, Mather, et al., 2023) have a 20 km grid spacing and are interpolated on a 7.5 km grid, matching the cell size of the inversion mesh, by applying statistical kriging using the python package PyKrig (Murphy et al., 2022), with a gaussian variogram and a nlags (Number of averaging bins for the semivariogram) value set to 20. After interpolation, the CPD map shows some values deeper than the Moho depths from (Pappa, Ebbing, & Ferraccioli, 2019) in the offshore area and along the coast. A CPD below the Moho would indicate that the upper mantle is magnetic and although this possibility has been suggested (Ferré et al., 2014)), we discard CPD values below the Moho boundary and in these areas use the Moho depth as the magnetic boundary depth (Figure 4b).

Both CPD and Moho depth have associated uncertainties. The CPD data set has reported uncertainties ranging between 2 and 6 km (Lowe, Mather, et al., 2023), while the uncertainty for the Moho depth ranges from roughly 5–8 km (Pappa, Ebbing, & Ferraccioli, 2019). Despite the uncertainty, it is beneficial to use physically derived estimates as the bottom boundary condition, rather than arbitrary selected constant boundary depths.

3. Method

3.1. Joint Inversion of Gravity and Magnetic Data

Joint inversion of gravity and magnetic data is carried out in JIF3D (Moorkamp et al., 2011). JIF3D is a 3D joint inversion framework for geophysical data sets including magnetotelluric, seismic, magnetic data, as well as scalar

and tensor gravity data. JIF3D utilizes a limited memory quasi-Newton approach (Avdeev & Avdeeva, 2009) for optimization. For a complete mathematical description of the JIF3D inversion framework the reader is referred to (Moorkamp, 2021, 2022; Moorkamp et al., 2011).

Inverting simultaneously for crustal density and susceptibility distribution using gravity and magnetic data in a joint inversion framework is well established (Bosch et al., 2006; Fregoso & Gallardo, 2009; Frey & Ebbing, 2020; Gallardo-Delgado et al., 2003; Guillen & Menichetti, 1984; Shamsipour et al., 2012). However, joint inversion based on VI, which allows the coupling of physical parameters, has only recently become popular in geophysical joint inversion applications (Haber & Holtzman Gazit, 2013; Lösing et al., 2022; Mandolesi & Jones, 2014; Moorkamp, 2021, 2022). VI is related to the concept of mutual information (MI) (Moorkamp et al., 2011). VI describes the amount of shared information contained in two variables, meaning a low VI value indicates that both variables are dependent, while a high VI value indicates that information about variable 1 does not reveal meaningful information about variable 2 (Lösing et al., 2022; Mandolesi & Jones, 2014; Moorkamp, 2021, 2022). VI is defined as:

$$VI(x,y) = 2H(x,y) - H(x) - H(y) \tag{1}$$

here $H(x) = -\sum_i p(x_i) \log p(x_i)$ is the Shannon Entropy; $p(x_i)$ is the probability density approximated by kernel methods (Mandolesi & Jones, 2014); $H(x)$ and $H(y)$ are the marginal entropies, and $H(x, y)$ is the joint entropy (Lösing et al., 2022; Moorkamp, 2021, 2022). VI is incorporated into the objective function Φ_{joint} as:

$$\Phi_{\text{joint}} = \Phi_{d,\text{grav}} + \Phi_{d,\text{mag}} + \lambda_1 \Phi_{\text{reg},\rho} + \lambda_2 \Phi_{\text{reg,sus}} + \lambda_3 \Phi_{\text{VI}} \tag{2}$$

where $\Phi_{d,\text{grav}}$ and $\Phi_{d,\text{mag}}$ are the Root-Mean-Square (RMS) misfit between observed and inverted gravity and magnetic data; $\Phi_{\text{reg},\rho}$ and $\Phi_{\text{reg,sus}}$ are regularization terms for the density and susceptibility distribution, controlling the smoothness of the inverted model. A full description of these terms can be found in (Moorkamp, 2021). Φ_{VI} is a coupling term which includes VI of recovered density and susceptibility and λ represents the weighting factors of the individual terms.

VI inversion has been successfully applied to magnetotelluric and seismic data (Mandolesi & Jones, 2014), magnetotelluric and gravity data (Moorkamp, 2021, 2022), and gravity and magnetic data (Lösing et al., 2022; Lösing et al., 2022) demonstrated that VI inversion can recover density and susceptibility distributions, if it is assumed that the gravity and magnetic signals have an identical source, by performing VI inversion tests on synthetic data.

3.2. Inversion Setup

The density and susceptibility inversion models are discretized into meshes with equal horizontal cell sizes of 7.5 km. The vertical cell size is 1 km at the surface and increases with depth by a factor 1.1 for each cell (Figure S3 in Supporting Information S1). Increasing vertical cell size with depth is introduced to account for decreasing resolution with increasing distance to the source in potential field applications. A horizontal cell size of 7.5 km is chosen because the input gravity and magnetic data have a grid spacing of 10 km (see Section 2). A cell size of 7.5 km allows the inversion to adjust on average more than one cell to fit the inversion data but is also not too small to not represent the point spacing of the input data or introduce artifacts. Additionally, a padding area of 20% around the study area is added to avoid edge effects. The resulting inversion mesh contains 244 cells in the grid-east to grid-west direction, 140 cells in the grid-north to grid-south direction and 21 cells in the z direction (above a maximum depth of 60 km below sea level). To constrain the model geometry, the bedrock topography from BedMachine version 3 (Morlighem et al., 2020), CPD (Lowe, Mather, et al., 2023), and Moho depths (Pappa, Ebbing, & Ferraccioli, 2019) are used. CPD and Moho depth estimation have their own associated uncertainties (see Section 2.4). The vertical increase of cells in the inversion mesh is an adaptation to account for those uncertainties. For example, at depths of the CPD of 24 km the vertical cell resolution is ∼3.5 km and at the Moho depth of 36.5 km the vertical resolution is ∼4.6 km representing uncertainties within both data sets used as model boundary conditions. Furthermore, competing Moho depth models for the study area (Baranov et al., 2021; Pappa, Ebbing, & Ferraccioli, 2019) report different Moho depths but the differences are less than 8 km (Figure

Table 1
Inversion Parameters

Coupling	25,000 run 1 and 15,000 run 2
Regularization density and susceptibility	10
Error gravity (mGal)	2 mGal
Error magnetics (nT)	15
Min./Max density (kg m^{-3})	±250
Min./Max susceptibility (SI)	±0.1
Magnetic field strength (nT)	64,981
Inclination (°)	−84.4
Declination (°)	147.4
dens_covmod (Maximum depth of density variation).	Moho depth
sus_covmod (Maximum depth of susceptibility variation).	CPD depth
coupling_validity (Maximum depth where coupling is assumed).	CPD depth

S4 in Supporting Information S1), which is of the order of magnitude of the uncertainties and the vertical cell resolution.

The aim of the VI inversion is to invert jointly the gravity and magnetic field for the density and susceptibility of the crust. Only cells between the bedrock interface and the Moho interface are allowed any variation during the inversion. However, rocks lose their magnetic properties at the Curie temperature. Therefore, joint VI inversion for both density and susceptibility is carried out only for cells between the bedrock interface and the CPD interface. Between the CPD interface and the Moho interface density only inversion is carried out and susceptibility is held at zero.

The input gravity field for the density inversion is corrected for masses below the Moho interface by the Antarctic lithospheric model from (Pappa, Ebbing, Ferraccioli, et al., 2019). All cells are set to a starting value of 0 kg/m^3 for the density anomaly model and 0 SI for the magnetic susceptibility model and are iteratively updated during the VI inversion process where they fall within the geometrically defined boundaries noted above.

The first inversion run is performed with a high coupling weight in order to enforce a tight coupling between the inverted models. Subsequently, a second inversion run is carried out, which uses the resulting density and susceptibility values from the first inversion run as a starting model, but a lower coupling weight is applied. The rationale behind using two different coupling weights is that a tighter coupling in the first inversion run favors geometrical structures in both the density and susceptibility, while a second inversion run with a lower coupling provides the inversion algorithm with more freedom to fit the observed gravity and magnetic field better (Moorkamp, 2022). Coupling values were established by trial and error.

The inducing magnetic field strength (Earths normal field) is set to 64,981 nT with a constant inclination of −84.4° and a declination of 147.4° for the whole study area based on the definitive magnetic reference field (DGRF) for a longitude of 155° and a latitude of −73° for the year 2005 (the year of the aerogeophysical survey WISE-ISODYN,the main survey in the study area). Additional parameter settings of the inversion are given in Table 1.

Subsequently the relationship between the inverted relative densities and susceptibilities are used to characterize 3D crustal structures and to identify crustal units with similar relationships.

4. Results

The VI inversion of gravity and magnetic data for the WSB and TAM region is carried out in two subsequent inversion runs with varying coupling factors of 25,000 for the first 100 iterations (inversion result shown in the Supporting Information S1 file) and 15,000 for subsequent 25 iterations, while all other parameters are kept fixed as described in Section 3.2 and Table 1. The Root Mean Square error (RMSE) after the combined 125 iterations is 1.5 mGal for the gravity inversion and 0.7 nT for the magnetic inversions (Figure 5a). VI increases sharply during
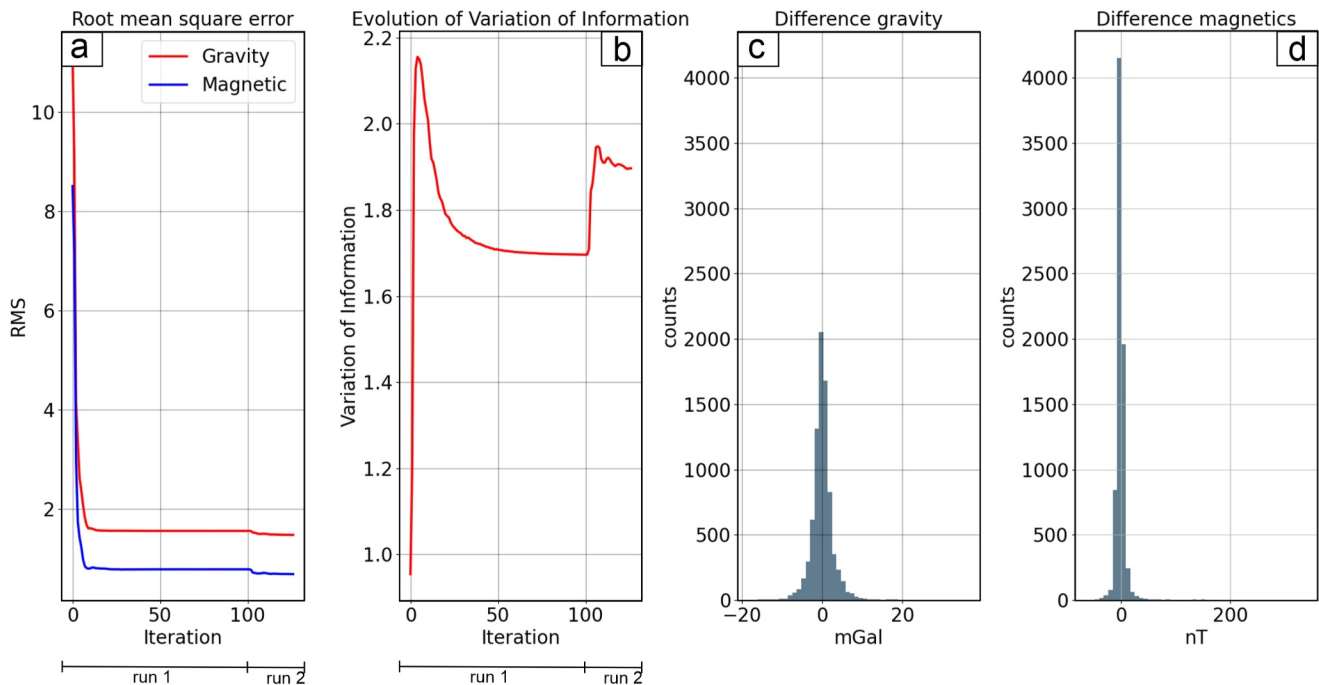
Figure 5. (a) Root mean square error between observed and inverted gravity (red) and magnetic (blue) field for each inversion iteration. (b) Evolution of variation of information (c) Gravity residual histogram between observed and inverted gravity field. (d) Magnetic residual between observed and inverted magnetic field.

the first inversion iterations, then decreases up until iteration 100.After the coupling is lowered at iteration 100, VI increases instantaneously, and decreases in the subsequent iterations (Figure 5b). A high value of VI means that susceptibility predictions from density and vice versa are more difficult. The coupling factors are highly data set specific. We run inversions with a range of coupling factors and choose the highest one that allows the inversion to converge to a satisfactory data fit. This produces the strongest coupled models that explain the data. As experience from other studies and this example show, it is not necessary to find an exact value, but values within a factor of two or so produce very similar results in practice (Franz et al., 2021; Lösing et al., 2022; Moorkamp, 2022). The RMS error decreases for the gravity and magnetic inversion sharply after the transition from a coupling of 25,000 to 15,000. Although the amplitude of the decrease in RMS error after lowering the coupling seems small, the long wavelength residual in the magnetic inversion model decreases significantly in the residual maps (Figure 6f and Figure S6 in Supporting Information S1)

The amplitude and distribution of anomalies within the gravity and magnetic field are reproduced well by the inversion (Figures 6a–6d). The end members of the residual between observed and inverted values are +37 and −18 mGal with a standard deviation of 3 mGal for the gravity inversion and +341 and −65 nT with a standard deviation of 13 nT for the magnetic inversion (Figures 5c and 5d). The difference map between observed and inverted values are shown in Figures 6e and 6f. Both residual maps show a good agreement between observed and inverted gravity and magnetic field with low residuals for most of the study area. The highest misfit amplitude in the gravity field is located in the area of the TAM, in the grid-southwest part of the study area. Airborne surveys are sparse in this area resulting in significant data gaps in the AntGG (Scheinert et al., 2016b) compilation. Gravity ground stations (Reitmayr et al., 2003; Zanutta et al., 2018) are used to fill the data gaps (Figure S1b in Supporting Information S1). A possible source of the higher amplitude in the misfit cluster in the TAM region could be contributed by the low spatial coverage of the ground stations and the offset in frequency content between the airborne and ground station data and could therefore be associated with local effects.

The largest misfits between the observed and inverted magnetic data are located around prominent data gaps within the WSB and the large data gap in grid-north, as well as in the gird-east of the study area, where the amplitude of the observed magnetic anomaly increases sharply from 300 nT to over 1,500 nT. It is expected that the inversion algorithm struggles to reproduce a rapid variation in the magnetic field of over 1,200 nT since the inversion algorithm favors smooth models. On the other hand, an error of 200 nT in a region with a field strength
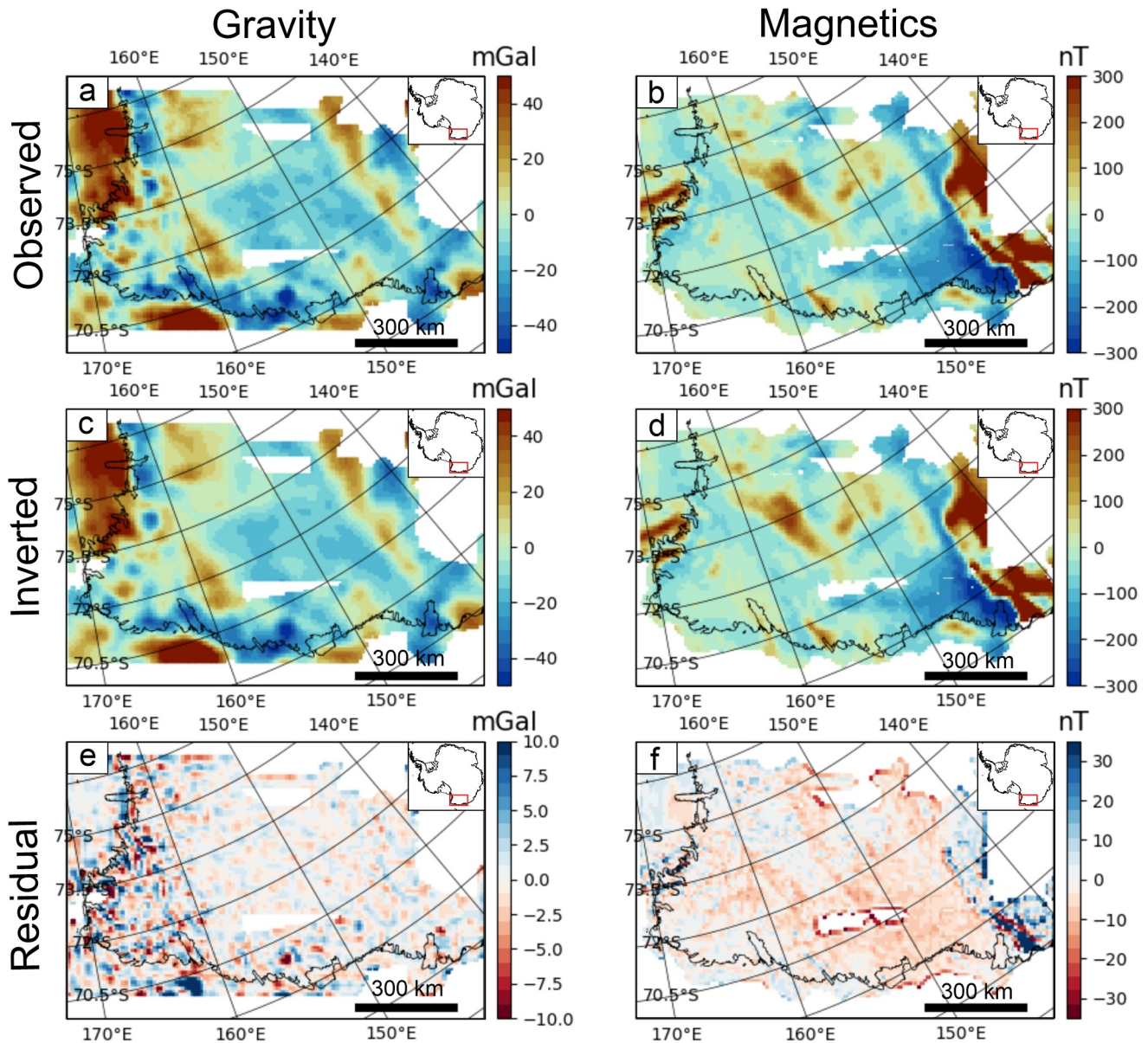
Figure 6. (a) Gravity inversion input data. (b) Magnetic inversion input data. (c) Final inverted gravity field. (d) Final inverted magnetic field. (e) Difference map between observed and inverted gravity fields (6a minus 6c). (f) Difference map between observed and inverted magnetic field (6b minus 6d).

of over 1,500 nT is less dramatic than compared to the TAM and WSB region with amplitudes of 300 nT. Additionally, a long wavelength feature exists in the magnetic residual map, which we don't further address due to the low magnitude below 5 nT.

Density and susceptibility depth slices at 5.5, 11.9, and 20.5 km depths are presented in Figure 7. The linear grid northwest-grid southeast anomaly in the central WSB (IB1) appears to be connected at depth with the neighboring anomaly with a grid northeast - grid southwest orientation (IB2), while both anomalies are separated at shallower depths.

The aim of the inversion is to find density and susceptibility distributions that are geometrically connected and simultaneously can explain the observed gravity and magnetic field. The underlying assumption is that a crustal rock has density and susceptibility values, which influence simultaneously the gravity and magnetic field. A cross section along profile AB (Figures 8a–8f) shows the similarities in the geometry of both petrophysical quantities. A large-scale negative density anomaly is located centrally in profile AB (black dotted circle in Figure 8b), while
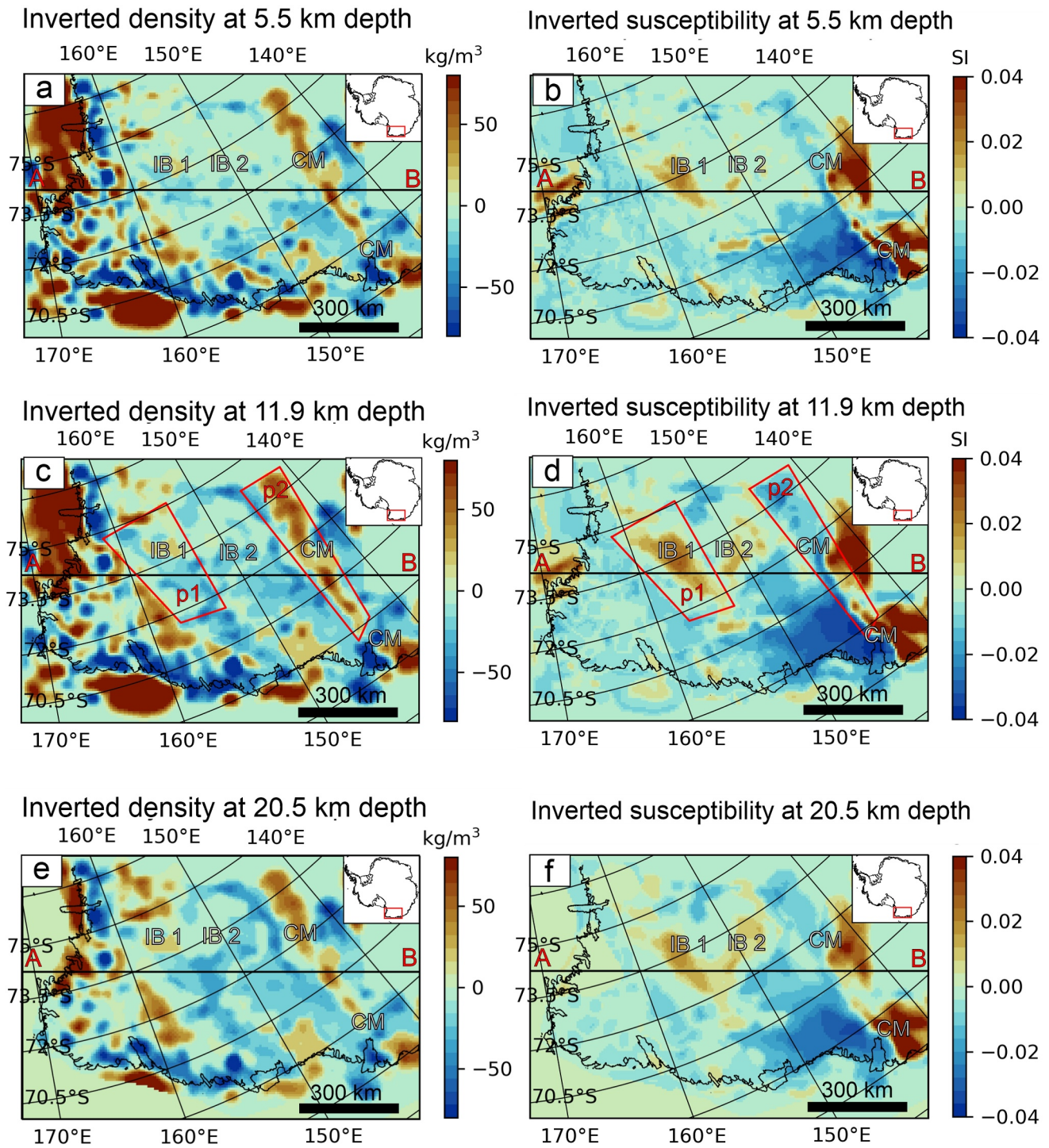
Figure 7. (a) Inverted density at 5.5 km depth. (b) Inverted susceptibility at 5.5 km depth. (c) Inverted density at 11.9 km depth. (d) Inverted susceptibility at 11.9 km depth. (e) Inverted density at 20.5 km depth. (f) Inverted susceptibility at 20.5 km depth. Black line indicates location of cross section profile in Figure 8. P1 and P2 indicate the polygons for extracting 3D distribution of density and susceptibility bodies. IB: intrusive body; CM: craton margin.

the susceptibility inversion model shows a high susceptibility anomaly with identical geometry. Adjacent to this anomaly is another negative density anomaly (red dotted circle in Figure 8b) but in this case the susceptibility values are also negative. This illustrates that a common geometry of both quantities is inverted, but the relationship between the density and susceptibility values is not linear. The cross section through the inverted density
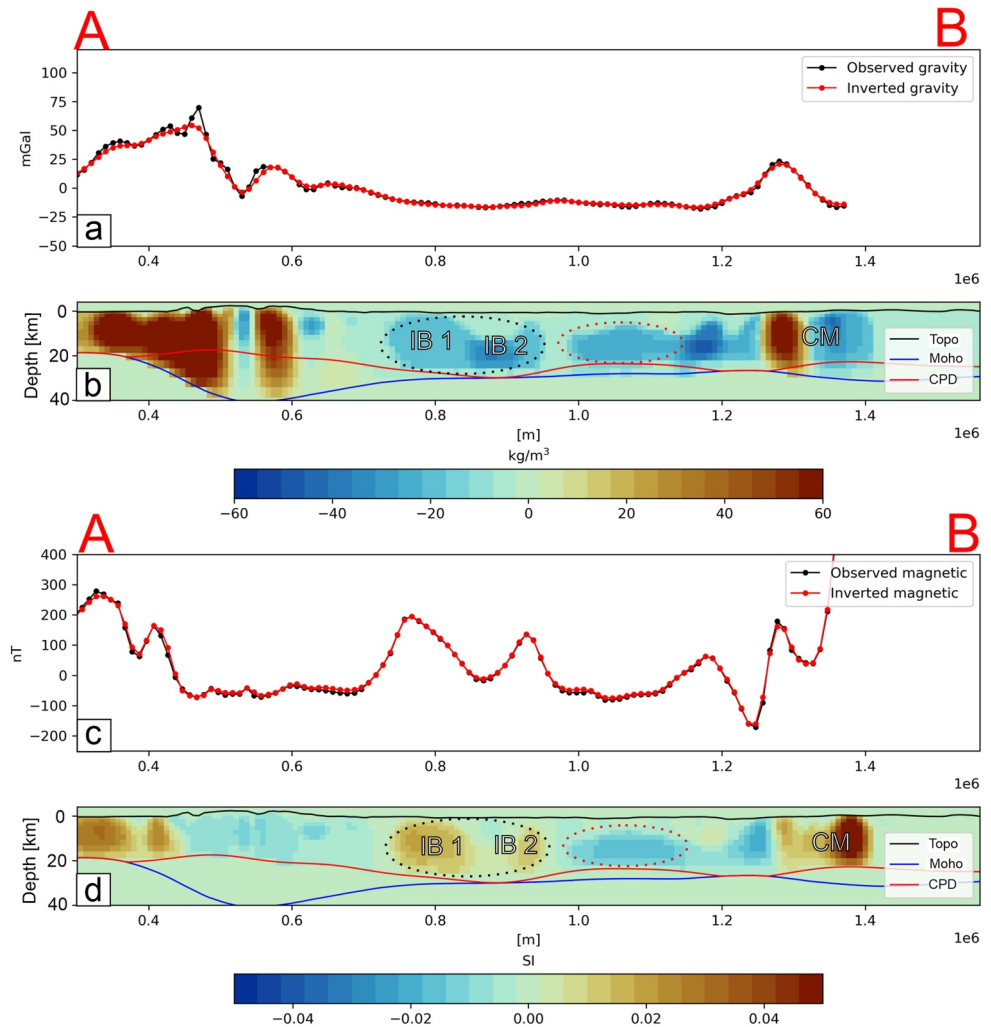
Figure 8. (a) Observed (black line) and inverted (red line) gravity field along profile AB. Location of profile AB is given in Figure 7. (b) Cross-section of the inverted density model along profile AB. (c) Observed (black line) and inverted (red line) magnetic field along profile AB. (d) Cross-section of the inverted susceptibility model along profile AB. IB: intrusive body; CM: craton margin.

and susceptibility model indicates that the source for the linear magnetic anomaly in the central WSB is connected at depth to the neighboring positive anomaly source with a perpendicular orientation (Figure 8). These results illustrate the advantage of using a joint inversion approach to obtain the density and susceptibility distribution (see Figures S6–S9 in Supporting Information S1).

4.1. Absence of Sediment Signature

The regional scale inversion results in the WSB do not show any clear signatures of sedimentary basins, such as broad regions of shallow low density material, lacking elevated magnetic susceptibility even though previous large geophysical efforts have been undertaken to identify sedimentary basins in the broader region of Wilkes Land (Aitken et al., 2014, 2023; Frederick et al., 2016). The absence of sediment basins in the inversion result might be due to a combination of factors. (a) A sedimentary layer thicker than 1 km may be absent, as suggested by previous magnetic depth to source and 2D gravity modeling in the WSB (Aitken et al., 2014; Frederick et al., 2016). (b) Well indurated sandstones, such as the Beacon Supergroup strata, can have densities hardly distinguishable to the surrounding crustal rocks. Measured densities of Beacon strata in northern Victoria Land range from 2,220 to 2,610 kg/m^3 (Barrett & Froggatt, 1978), coming close to the crustal average of 2,670 kg/m3 assumed in the model. The close association of Beacon sandstones with intrusive Ferrar dolerites observed in
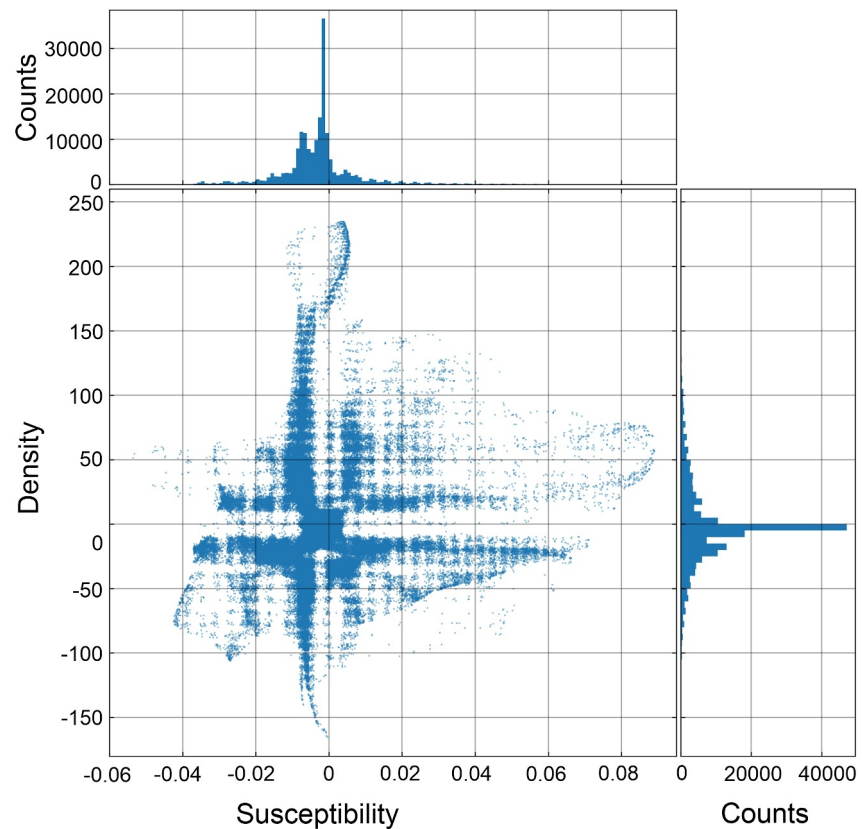
Figure 9. Inverted density and susceptibility cross plot and density and susceptibility histograms of the Variation of Information inversion model.

outcrop (Goodge & Finn, 2010) may further mask the presence of a sedimentary basin, as the intrusive rocks both increase the mean density and increase the apparent susceptibility of the associated crustal volume. (c) The vertical inversion mesh resolution increases with depth and at the depth of the upper crust the vertical cell size is ~1,200 m while the horizontal resolution is 7,500 m. In order to recover a low-density sediment layer, the layer must fill the majority of an inversion cell (1,200 m times 7,500 m times 7,500 m). Evidence of sediments layer thicker than 1,200 m is currently lacking (see above).

4.2. Density and Susceptibility Relationship

A density and susceptibility cross plot illustrate the parameter relationship between both quantities (Figure 9). The relative inverted densities range from −160 to 250 kg/m^3, while the inverted susceptibilities range from −0.06 to 0.9 SI. However, the density and susceptibility histograms indicate that the inverted density values are predominantly between ±50 kg/m^3 and inverted susceptibility values are mostly between ±0.02 SI.

High relative density values above 100 kg/m^3 are located exclusively offshore, while large negative values below −100 kg/m^3 are located as distinct clusters in the TAM and along the coast (Figures 10a and 10b). High relative susceptibility values above 0.025 SI are located offshore and to a much larger extent at the grid-eastern edge of the WSB at the inferred CM (Figures 10a and 10b). Furthermore, strong negative relative susceptibility values below −0.03 SI are limited to the CM (Figures 10a and 10b).

To constrain the geometry and properties of particular sub-surface source bodies we extracted the inverted density and susceptibility values within the polygons p1 and p2 (polygon location shown in Figures 7c and 7d) and subsequently used thresholding of the susceptibility or density values to recover the approximate geometry of sources associated with specific anomalies. The source for the prominent positive magnetic anomaly in the WSB region is extracted by windowing the joint inversion output in this area for relative susceptibility values larger than 0.003 SI. The volume of the extracted body amounts to ~286,000 km^3. The source for the linear high gravity
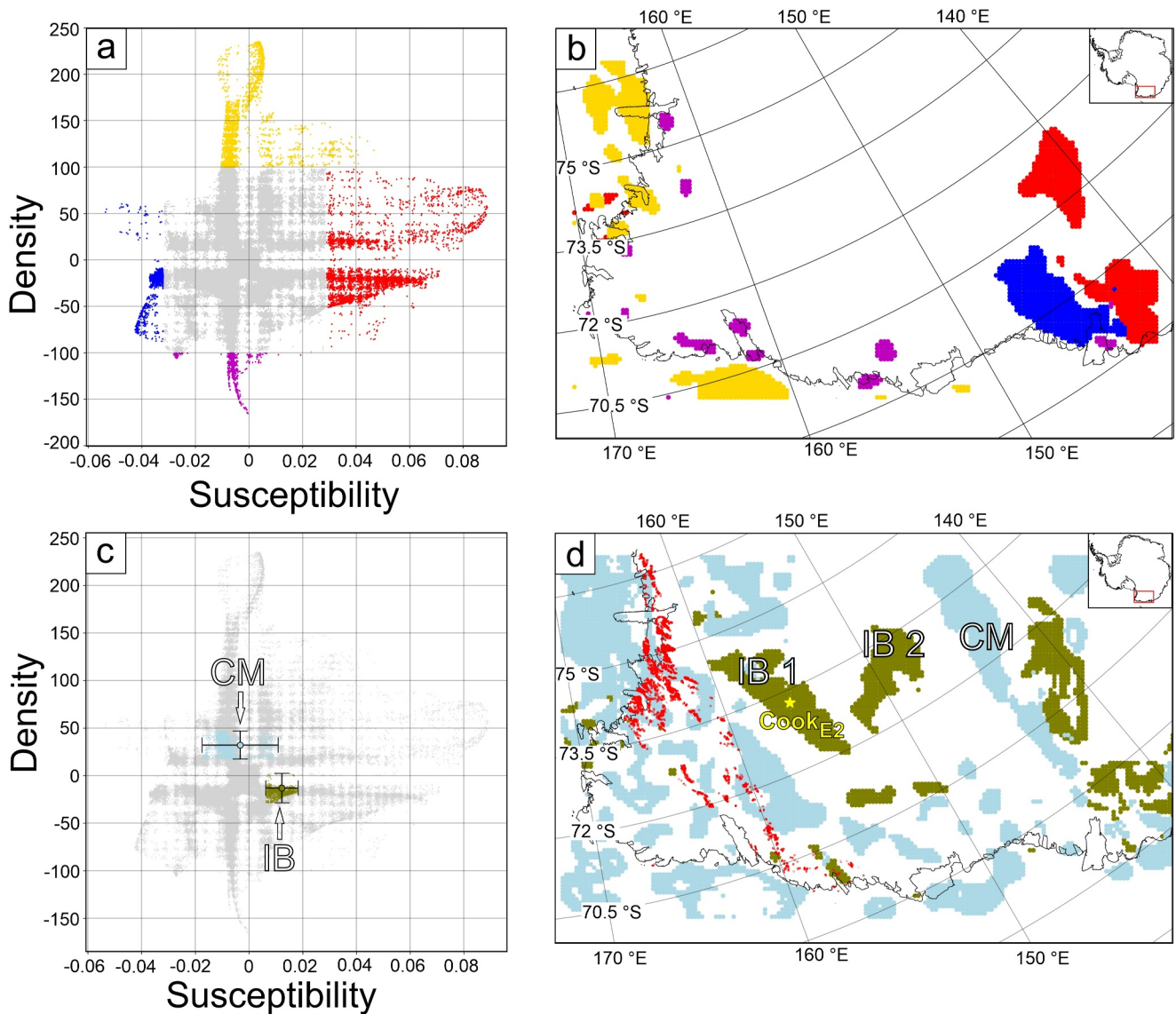
Figure 10. Density versus susceptibility cross-plots and province characterization. (a) Extreme susceptibility and density groupings. High inverted relative density values above 100 kg/m^3 (yellow dots), low relative inverted density values below—100 kg/m^3 (purple dots), high relative inverted susceptibility values above 0.029 SI (red dots) and low relative inverted susceptibility values below −0.032 SI (blue dots) superimposed on density and susceptibility cross-plot of the entire inversion model. (b) Spatial distribution of extreme density and susceptibilities highlighted in panel (a). (c) Mean and standard deviation (error bars) of interpreted intrusive body (olive green) and craton margin feature (pale blue) isolated using thresholding of standard deviation of recovered values within p1 and p2 located in Figure 7. All recovered values falling within the recovered density/susceptibility ranges are color coded accordingly and superimposed on density and susceptibility cross-plot of the entire inversion model. (d) Location plot of density and susceptibility relationships within the standard deviation range of the extracted bodies in Figure 10c. Granite Harbor Intrusive Complex (red) taken from GeoMAP (Cox et al., 2023a). IB: intrusive body; CM: craton margin. Yellow star location of Cook$_{E2}$ subglacial lake.

anomaly on the grid-eastern flank of the WSB was extracted by windowing the joint inversion output in this area for relative density values larger than 10 kg/m^3. The mean and standard deviation of the density and susceptibility relationship within those two extracted prominent bodies are superimposed on the density–susceptibility cross plot of the whole inversion model (Figure 10c). Both features cluster around distinct areas in the cross plot and are easily distinguishable (Figure 10c). The Central WSB source (IB1) has a mean relative density that is slightly negative (−13.1 kg/m^3) and a mean relative susceptibility that is moderately positive (0.012 SI), while the mean relative density is positive (32.1 kg/m^3), and the mean relative susceptibility is negative (−0.003 SI) for the feature along the CM. The standard deviation for the susceptibility of the CM feature is significantly larger compared to the intrusion signal (Figure 10c). The standard deviation range of density and susceptibility for each
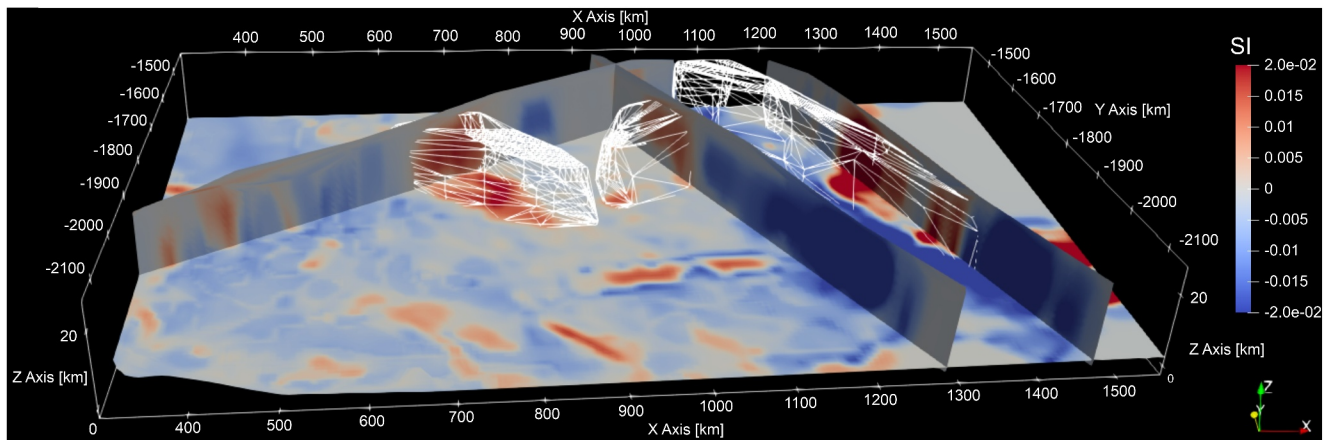
Figure 11. 3D intrusion and craton margin (CM) bodies (white wireframe) superimposed on slices through the 3D inverted susceptibility model. View looking grid north (approximately south south west geographically) along the axis of the Wilkes Subglacial Basin, with two interpreted intrusive bodies in the center and CM source body to the right. *X*, *Y*, and *Z* axis in km. *Z* axis vertical scaled by a factor of 5.

body is subsequently used to filter the entire inversion model to find the location of rocks with matching density and susceptibility relationships across the study area (Figure 10d). The location of rocks with matching susceptibility and density relationships reveals petrophysical similarities between the central WSB magnetic anomaly (F1 in Figure 3) and the adjacent magnetic anomaly that lies perpendicular to it (F2 in Figure 3), which potentially has the same origin (IB1, IB2 in Figure 10d). The extent and volume of those 3D structures can be extracted from the model (Figure 11).

5. Interpretation and Discussion

Our new inversion provides insights into the geometry and petrophysical properties of the bodies beneath the WSB. As a result of an inversion of geophysical data it is, by its nature, non-unique. However, by combining magnetic and gravity data we have provided a more constrained model, consistent with both data sets, compared to previous studies, which relied on 2D models of either gravity or magnetic data in this region (Ferraccioli, Armadillo, Jordan, et al., 2009; Jordan et al., 2013). The recovered pattern of density and susceptibility is considered robust and reveals more geologically reasonable structures compared to inverting for both quantities independently (see in Supporting Information S1) and, therefore, can provide improved insights about the underlying geology. The uncertainty in boundary conditions (CPD and Moho depth) might influence the recovered density and susceptibility values in terms of amplitude, but the horizontal spatial distribution is less effected. Furthermore, the lack of external constraints such as seismic receiver function, seismic reflection methods, or crustal wave velocities does not allow us to reduce the non-uniqueness of potential field data, meaning thickness remains an estimate. It is possible that the complex superposition of bodies of varying susceptibility and density could also yield a very different structural model fitting the data equally well, but without evidence for this, we believe our inversion output to be a reasonable starting point for a discussion of the subglacial geology.

5.1. Batholith Location, Age, and Potential Significance

One of the most obvious features of the inversion result is the identification of a large body with elevated susceptibility and slightly negative density values (mean 13 kg/m^3), which are confined to a narrow range of 30 kg/m^3 in the center of the WSB. We interpret this body as a large-scale igneous batholith. Shifting the relative density values to absolute values by adding the average crustal background density of 2,670 kg/m^3 indicates that the density of the extracted body in the center of the WSB ranges from 2,620 to 2,670 kg/m^3 combined with susceptibility values moderately above the general values for the region. Shifting relative susceptibility values to absolute values is more challenging compared to the density counterpart because i) no crustal susceptibility background value exists ii) the inverted susceptibility includes remanent, the impact of magnetization which translates as relative susceptibility values which may be negative. However, the susceptibility values from our inversion show a strong peak close to zero, which we take as the crustal background, while relatively positive susceptibility values are taken as an approximation of true rock susceptibility. The density and susceptibility

relationship is in accordance with the petrophysical relationship for granite rock samples from Australia (Barlow, 2004) and from the south Indian shield (Subrahmanyam & Verma, 1981) illustrated by (Lösing et al., 2022). However, it should be noted that susceptibility ranges for different lithologies overlap, and even within the same rock type there can be a large internal variability (Lowe et al., 2024). Granodiorite and other granitoid composition (e.g., tonalite, diorite) plutons fit comfortably within the susceptibility range as well. Susceptibility ranges from granites of the Cambro-Ordovician Granite Harbor intrusive complex are reported to be between 0.002 and 0.08 SI, while the majority of values are between 0.001 and 0.01 SI (Bozzo et al., 1992; Ohneiser et al., 2015). Significantly lower susceptibility values are reported for Ordovician granitoids of northern Victoria Land (0.00668 SI) (Bozzo et al., 1992; Lanza & Tonarini, 1998). The mean susceptibility recovered for the central WSB body is 0.012 SI. Although reasonable for a granite (Barlow, 2004; Maslanyj et al., 1991; Subrahmanyam & Verma, 1981), it is above values often quoted for the Granite Harbor intrusive rocks (Bozzo et al., 1992, 1995; Goodge & Finn, 2010; Ohneiser et al., 2015). We therefore suggest that the central WSB body is distinct from the exposed Granite Harbour Intrusive rocks.

The large-scale igneous batholith identified here (IB1) has an identical petrophysical signature in terms of density and susceptibility as the neighboring body labeled IB2 in Figure 10d, which is associated with the magnetic anomaly labeled F2 in Figures 3a and 3b. The density and susceptibility distribution along the profile AB (Figures 8b and 8d) and the depth slices (Figure 7) indicate that these intrusive bodies (IB1 and IB2) may be connected at depth. The total combined volume of the proposed batholith IB1 and IB2 is ~470,000 km^3, which constitutes a significant addition to the volume of the upper crust at the time of emplacement. However, this estimation is likely an upper bound on the volume estimation since the base of any intrusion is poorly resolved by gravity and magnetic methods, and constraints on crustal boundaries (CPD and Moho depth) are uncertain, hence thickness estimations are likely to be exaggerated. Granites often form topographic highlands in glacial regions due to their relative resistance to erosion compared to surrounding sediments, but this is not clearly seen in the WSB. IB1 is flanked by a deep trough parallel to the inferred geological contact indicating geological control of erosion on one flank, and that the intrusion may be at the ice bed interface in this area. In many other areas the topography shows no clear change at the geological boundary of IB1 or IB2, which may indicate the intrusive bodies remain at least partially buried.

The petrophysical signature of IB1 and IB2, in terms of jointly inverted density and susceptibility relationship is not present in the TAM region. This is perhaps surprising, since granites from the Granite Harbor Igneous Complex are mapped and sampled by geological surveys in this area (Cox et al., 2023a). This suggests that the petrophysical signature of the proposed batholithic is fundamentally different to the lithologies of the Granite Harbor Igneous Complex (Figure 10d, red dots), which was emplaced during the later stages of the Ross Orogeny (Estrada et al., 2016). We cannot know the age of emplacement of the IB1 and IB2 bodies and can only speculate that they may also be associated with magmatism of the Ross Orogeny. However, their position, which is more proximal to the continental interior, suggests that they may record an episode of older arc-related magmatism relative to the Granite Harbor Igneous Complex, as arc systems often migrate outboard toward the adjacent trench through time (Gianni & Luján, 2021). We speculate that the batholith in the central WSB was emplaced during an early phase of the Ross Orogeny and maybe the source of the >550 Ma zircons in the Priestley Formation (Estrada et al., 2016), and also in the WSB basement adjacent to the Mertz Shear Zone, sampled as xenoliths in later ~500 Ma granites (Lamarque et al., 2018).

The crustal-level intrusive bodies are interpreted as a batholith, and potentially reach depths of 20–25 km, which represents the maximum extent of batholiths reported worldwide, but is also not unprecedented. As the Pacific Margin Anomaly (PMA) batholith in the central Antarctic Peninsula is predicted to reach 20 km depth (Ducea, 2001; Johnson, 1999; Saleeby et al., 2003) determined the thickness of the Sierra Nevada batholith must have been ~30–35 km prior to erosion. However, we acknowledge the inversion model is likely to overestimate the source thickness of this body due to a combination of factors, including loss of resolution with increasing distance between sensor and source for potential field data, uncertainty in CPD and Moho depth estimation. A lack of independent crustal parameters such as receiver functions, or active and passive seismic experiments limit the possibility to validate the geophysical inversion. Therefore, the batholith might be thinner than predicted by our regional scale joint inversion.

A batholithic intrusion, even if 5–10 km thinner, still represents a significant local crustal feature, which would influence the GHF of the region if it acted to concentrate radiogenic elements. Even though the lack of direct

geological samples and heat flow measurements makes it challenging to quantify the extent of this impact, many granitic batholiths are associated with elevated heat production, with global late Proterozoic granites typically higher in heat producing elements (U, Th, K) than Phanerozoic granites (Artemieva et al., 2017). The batholith we have imaged is, therefore, likely to generate a locally elevated GHF and this impact may be quite marked for this sector of East Antarctica where heat flow values are rarely predicted to exceed ∼60 mW/m^2 (An et al., 2015; Fox Maule et al., 2005; Haeger et al., 2022; Lösing & Ebbing, 2021b; Lowe, Mather, et al., 2023; Martos et al., 2017, 2017b; Shen et al., 2020; Stål et al., 2021). The magnitude of the heat flow anomaly is unknown but the batholith in our model is of a similar size to the ∼200 km long Cornubian batholith in south west (SW) England, where heat flow of up to 138 mW/m^2 is reported (Beamish & Busby, 2016). This comparison illustrates that heat flow is potentially underestimated in geophysical GHF models if the crustal domain is treated with global average values instead of accounting for crustal heterogeneities recovered from geophysical data.
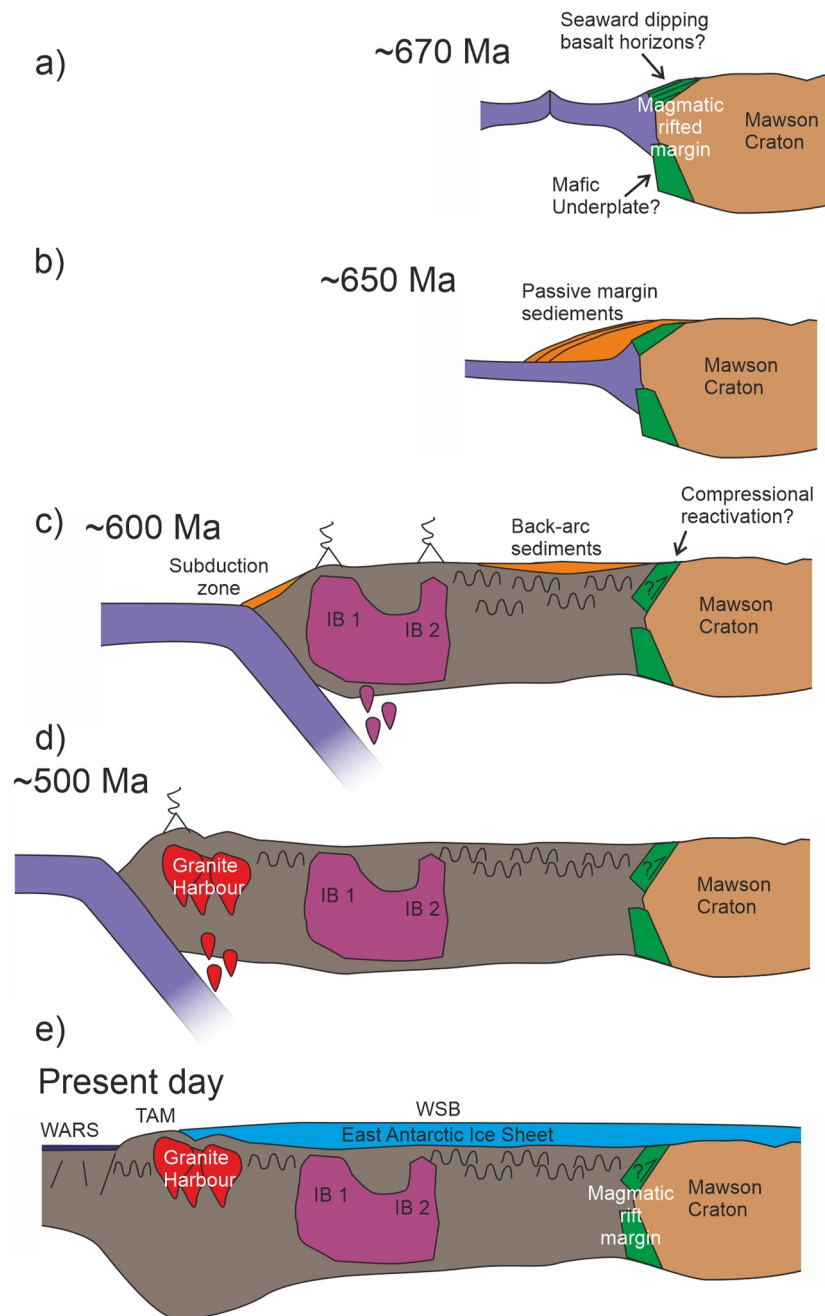
5.2. Continental Margin

The density and susceptibility relationship for the linear structure at the CM is more ambiguous than the proposed batholith structures, due to the larger standard deviation in the susceptibility values. Similar density and susceptibility relationships are present offshore and onshore along the coast and in the TAM, but these areas may be lithologically and tectonically distinct from the CM structure.

There are several potential tectonic models for the high density bodies recovered along the inboard margin of the WSB, which is interpreted to represent the margin of the Mawson Craton (Goodge & Finn, 2010). One hypothesis is that the positive gravity anomaly is a slice of up-thrusted crustal material loading the CM (Studinger et al., 2004). However, our inversion modeling does not show the strongly asymmetric pattern of densities expected for a flexural loaded margin, although we cannot rule out some degree of compressional re-working of the former rifted margin during the Ross Orogeny. An alternative model is that the observed gravity and magnetic anomalies are directly associated with processes occurring along the rifted margin. Along strike, in the Glenelg River Complex of south east Australia, it is proposed that slivers of ultramafic rocks associated with a magma-depleted hyperextended Rodinian continental margin are present, which were re-worked by later compressive orogenic forces (Gibson et al., 2015). Although associated with similar margin parallel magnetic anomalies, the amplitude of the magnetic anomalies directly associated with the Australian ultra-mafic rocks are often lower amplitude and more fragmented than observed in Antarctica. In addition, the interpreted Australian ultra-mafic rocks are not associated with a distinct positive gravity anomaly as seen in the WSB. If the WSB margin does reflect the relics of a magma-poor margin, we propose that it must be more intact than that in Australia to account for the very significant source bodies recovered by the inversion. As an alternative, the linear CM feature may be the signature of a former magmatic rifted continental margin where thick sequences of seaward-dipping basalt horizons are often combined with mafic underplating (Direen & Crawford, 2003). Both features require densities above 2,700 kg/m^3, in line with the inversion result. Additionally, both features host the potential of significant remanent magnetization, as suggested by the recovered negative relative susceptibility. We prefer a magmatic, rather than an amagmatic margin model given the scale and amplitude of the observed magnetic and gravity anomalies. The presence of magmatic features associated with rifting would not be unexpected given the location on the former cratonic margin, and is not incompatible with magma-poor rifting interpreted on other parts of the margin (Gibson et al., 2015). Ultimately, a more detailed geophysical study is required to definitively reveal the nature of the margin.

5.3. Conceptual Tectonic Model

Based on our preferred interpretation of the inversion outputs and the regional geological context we propose a tentative geotectonic model for the evolution of the WSB (Figure 12):

The first identified event is linked to continental breakup leading to the development of margin parallel gravity and magnetic anomalies, which we attribute to a magmatic rifted margin adjacent to the Mawson Craton with seaward-dipping basalt horizons and mafic underplating (Figure 12a). The age of breakup is uncertain, but evidence of rifting and passive margin development along strike in the Central TAM suggests that this may have occurred around 670 Ma (Goodge, 2020; Goodge et al., 2002). Rifting would have been followed by the development of a passive margin sequence and progressive subsidence (Figure 12b).

Figure 12. Conceptual tectonic evolution sketch: (a) Rifting of Rodinia supercontinent and development of magmatic margin. (b) Passive margin development and sediment deposition. (c) Subduction zone development, emplacement of Central Batholith, re-working of passive margin and potentially deposition of back-arc sediments. (d) Subduction zone migrates further out-board and Granite Harbor intrusive suite is emplaced. (e) Present day geological section.

Margin inversion and development of an ocean/continent subduction system and associated continental margin arc, led to the emplacement of the large-scale batholithic intrusions, IB1 and IB2 in the central WSB area (Figure 12c). Potential re-working and back thrusting of mafic components onto the CM may have also occurred at this time. The emplacement age of this proposed phase of arc magmatism is uncertain, but we suggest it pre-dated the main phase of Ross Orogeny magmatism exposed as the Granite Harbor Intrusive suite in the TAM. As such, this earlier phase of magmatism could provide a local source for >550 ma detrital zircons of otherwise unknown provenance (Estrada et al., 2016). An early Ross Orogeny phase of magmatism has also been proposed

in the central TAM, with the earlier phase of magmatism generally being focused further inboard (Goodge, 2020; Goodge et al., 2024). Although slightly younger than the detrital evidence, this central TAM interpretation is consistent with our early Ross model for development of IB1 and IB2. Later Ross magmatism led to the emplacement of the Granite Harbor Igneous Complex ~500 Ma, further outboard from the CM, in the region of the present-day TAM (Figure 12d).

5.4. Cryosphere Implication

GHF in Antarctica is understood to be an important solid earth contribution to the cryosphere (Livingstone et al., 2022; Reading et al., 2022; Siegert & Dowdeswell, 1996). GHF is the dominant heat source close to the ice divides (Bell, 2008; Fahnestock et al., 2001; Siegert & Dowdeswell, 1996), whilst away from the ice divides, horizontal ice deformation and basal sliding become the dominant sources. A causal link between subglacial lakes and high GHF has been proposed by several authors (Fahnestock et al., 2001; Fisher et al., 2015). A prominent active subglacial lake several tens to hundred meters deep called $Cook_{E2}$ close to the ice divide (Y Li et al., 2020; McMillan et al., 2013; B. E Smith et al., 2009) is located directly above the modeled batholith IB1 (Figure 10d). The ice surface above subglacial lake $Cook_{E2}$ exhibited surface subsidence of 70 m between 2006 and 2008 (observed by CryoSat-2), which has been linked to a discharge event. Following the lake discharge, it has been recharging at a rate of 5.6 ± 2.8 m yr^{-1} (McMillan et al., 2013). It is notable that almost all recent GHF models (An et al., 2015; Lowe, Mather, et al., 2023; Martos et al., 2017, 2017b; Shen et al., 2020; Stål et al., 2021), with the exception of (Lösing & Ebbing, 2021b) predict a local GHF minimum in the lake location above IB1 (Figure S12 in Supporting Information S1). This is a consequence of all recent GHF models have in common that they are simplifying the local crust to a set of constant petrophysical values or neglect any heterogeneity in the subglacial geology. It is possible, given the spatial overlap, that the $Cook_{E2}$ lake could be induced by a thermal anomaly associated with the IB1 batholith and high concentration of heat producing elements. This highlights the necessity of GHF models to incorporate subglacial and crustal heterogeneities where data is available, also suggested in recent papers (Li & Aitken, 2024; Lowe et al., 2024; Stål et al., 2024). It is important to note that not all subglacial lakes can be correlated to regions of high GHF. Subglacial lakes serve at best as a weak proxy for elevated heat flow, since basal melt may have undergone lateral transport to the accumulation region or even refreeze during transport. However, it is notable that in the case of $Cook_{E2}$ a subglacial lake up to several hundred meters deep is located above the batholith IB1, which is likely to elevate the local heat flow. It is important to stress that the proposed batholith in this study is a geological interpretation based on airborne geophysical data and classifying this structure based on inverted petrophysical relationship as a granite-like rock type is somewhat speculative. Coupling this consideration with the poorly constrained heat flow models, the existence of the lake cannot be tied to the intrusive rock body with certainty and emphasizes important questions that future studies should consider for studying solid earth and cryosphere interactions.

6. Conclusions and Future Work

We present a density and susceptibility distribution model for the WSB and the TAM using joint inversion of gravity and magnetic data based on VI coupling. This model provides insight into the heterogeneity of the 3D crustal structure in the WSB and TAM region and allows preliminary quantification of the volume of crustal provinces, which should be considered in future lithospheric scale thermal studies. The inversion model images a large body of slightly low density and moderately positive susceptibility values in the central WSB, which we interpret as a large-scale batholith. Based on the inverted petrophysical properties the batholith is interpreted as being granitic in composition, but it is not currently possible to further constrain the specific lithology. The density and susceptibility relationship and cross-section of the inversion model indicates that this structure is connected to the adjacent low density moderate susceptibility body, which potentially has the same origin but nearly perpendicular orientation. If so, the volume of the total granitic intrusive body increases to ~470,000 km^3, which is a considerable addition to the volume of the upper crust at the time of emplacement and has the potential to have a significant impact on the local heat flow due to the likely concentration of radiogenic heat producing elements. However, the thickness of the batholith and the volume is dependent upon the boundary conditions, especially the CPD, with significant uncertainties and therefore the thickness and volume may represent an overestimate. Despite the absence of direct heat production and heat flow measurements, comparisons with well-studied granite intrusion provinces in the Weddell Sea (Leat et al., 2018), southern Prydz Bay (Carson

et al., 2014), SW England (Beamish & Busby, 2016) and worldwide (Artemieva et al., 2017) emphasize the influence that local crustal structures such as granitic intrusive bodies can have on the local heat flow budget.

Examining the density and susceptibility relationships, we have determined that the batholith has a different petrophysical signature to the Granite Harbor Intrusive Complex of the TAM. Based on our findings, the tectonic evolution of the WSB may therefore include two distinct intrusion events, first emplacement of the batholith followed by the emplacement of the Granite Harbor Intrusive Complex. The batholith emplacement age is uncertain and may represent an episode of magmatism associated with the early stages of the Ross Orogeny (c. 600 Ma) or could potentially be associated with rift-margin processes in the interval, 650–670 Ma (Goodge et al., 2012). This could potentially provide a more proximal source for the Neoproterozoic clasts described from meta conglomerates of southern Victoria Land (Cooper et al., 2011).

The margin of the Mawson craton is identified by the inversion in the form of a positive linear gravity anomaly grid-east of the WSB. We suggest these signatures reflect a former passive continental margin with thick seaward-dipping basalt horizons and mafic underplating. However, alternative models of up-thrusted crustal material at the craton edge, or re-working of ultramafic material from a magma-poor rifted margin cannot be ruled out based on the geophysical inversion model. Scenarios combining some of these endmember models are also possible.

This study highlights the crustal heterogeneities on a regional scale in East Antarctica and provides evidence that use of a set of constant global average petrophysical values for the crustal domain in geophysical GHF models is a simplification that might underestimate the contribution of GHF beneath the ice sheets. Despite the many challenges, next generation geophysical heat flow models are required to consider crustal heterogeneities to increase the understanding of the contribution from the solid earth to the cryosphere dynamics and ultimately the stability of the ice sheet. Therefore, further geophysical, and geological research on the Antarctic subglacial geology is necessary to understand the thermal state of the most remote continent on Earth.

Data Availability Statement

The inverted density and susceptibility model, the resulting gravity and magnetic response as well as the input gravity and magnetic data for the inversion is published through the UK Polar Data Centre (Lowe, Jordan, et al., 2023). Python code in form of a Jupyter notebooks to reproduce the inversion and plot the inversion results are published through Zenodo (Lowe, 2023). Bedrock topography taken from "BedMachine Antarctica version 3" (Morlighem et al., 2022). Magnetic data taken from "ADMAP-2" (Golynsky et al., 2018a). Gravity data taken from "AntGG" (Scheinert et al., 2016a). Additional gravity data are taken from data tables from (Reitmayr et al., 2003; Zanutta et al., 2018). Curie point depths data taken from (Lowe et al., 2022). Moho depths taken from the Supporting Information of (Pappa, Ebbing, & Ferraccioli, 2019). Geological units taken from GeoMAP (Cox et al., 2023b). Geothermal heat flow models presented in the Supporting Information file taken from: (An et al., 2015; Lösing & Ebbing, 2021a; Lowe et al., 2022; Martos et al., 2017a; Shen et al., 2020; Stål et al., 2020), Software—The joint inversion was carried out using JIF3D (Moorkamp et al., 2023). Furthermore, the commercial software Oasis Montaj (Seequent; Reading, England) was used to for gridding data, upward continue gravity and magnetic grids, accessing the ADMAP-2 data complication as well as data plotting. Additionally: the following python packages were used: NumPy (Harris et al., 2020), Matplotlib (Hunter, 2007); Pandas (McKinney, 2010); Geopandas (Jordahl et al., 2020); Cmrameri (Crameri, 2023); Cartopy (Elson et al., 2022); Shapley (Gillies et al., 2022); SciPy (Virtanen et al., 2020); PyKrige (Murphy et al., 2022) and Jupyter notebook (Kluyver et al., 2016).

References

Aitken, A. R. A., Li, L., Kulessa, B., Schroeder, D., Jordan, T. A., Whittaker, J. M., et al. (2023). Antarctic sedimentary basins and their influence on ice-sheet dynamics. *Reviews of Geophysics*, *61*(3), e2021RG000767. https://doi.org/10.1029/2021RG000767

Aitken, A. R. A., Young, D. A., Ferraccioli, F., Betts, P. G., Greenbaum, J. S., Richter, T. G., et al. (2014). The subglacial geology of Wilkes Land, East Antarctica. *Geophysical Research Letters*, *41*(7), 2390–2400. https://doi.org/10.1002/2014GL059405

An, M., Wiens, D. A., Zhao, Y., Feng, M., Nyblade, A., Kanao, M., et al. (2015). Temperature, lithosphere-asthenosphere boundary, and heat flux beneath the Antarctic Plate inferred from seismic velocities. *Journal of Geophysical Research: Solid Earth*, *120*(12), 8720–8742. https://doi.org/10.1002/2015JB011917

Artemieva, I. M., & Mooney, W. D. (2001). Thermal thickness and evolution of precambrian lithosphere: A global study. *Journal of Geophysical Research*, *106*(B8), 16387–16414. https://doi.org/10.1029/2000JB900439

Artemieva, I. M., Thybo, H., Jakobsen, K., Sørensen, N. K., & Nielsen, L. S. K. (2017). Heat production in granitic rocks: Global analysis based on a new data compilation GRANITE2017. *Earth-Science Reviews*, *172*, 1–26. https://doi.org/10.1016/j.earscirev.2017.07.003

Avdeev, D., & Avdeeva, A. (2009). 3D magnetotelluric inversion using a limited-memory quasi-Newton optimization. *Geophysics*, *74*(3), F45–F57. https://doi.org/10.1190/1.3114023

Baranov, A., Tenzer, R., & Morelli, A. (2021). Updated Antarctic crustal model. *Gondwana Research*, *89*, 1–18. https://doi.org/10.1016/j.gr.2020.08.010

Barlow, M. (2004). *Density and susceptibility characterization of major rock units and rock types of mount isa inlier i1 and i2 projects pmd∗CRC internal report*. Commonwealth of Australia. Retrieved from https://ecat.ga.gov.au/geonetwork/srv/api/records/a05f7892-da0b-7506-e044-00144fdd4fa6

Barrett, P. J., & Froggatt, P. C. (1978). Densities, porosities, and seismic velocities of some rocks from Victoria Land, Antarctica. *New Zealand Journal of Geology and Geophysics*, *21*(2), 175–187. https://doi.org/10.1080/00288306.1978.10424049

Beamish, D., & Busby, J. (2016). The cornubian geothermal province: Heat production and flow in SW England: Estimates from boreholes and airborne gamma-ray measurements. *Geothermal Energy*, *4*(1), 4. https://doi.org/10.1186/s40517-016-0046-8

Bell, R. E. (2008). The role of subglacial water in ice-sheet mass balance. *Nature Geoscience*, *1*(5), 297–304. https://doi.org/10.1038/ngeo186

Bialas, R. W., Buck, W. R., Studinger, M., & Fitzgerald, P. G. (2007). Plateau collapse model for the transantarctic mountains–West Antarctic rift system: Insights from numerical experiments. *Geology*, *35*(8), 687–690. https://doi.org/10.1130/g23825a.1

Blakely, R. J. (1996). *Potential theory in gravity and magnetic applications*. Cambridge university press.

Block, A. E., Bell, R. E., & Studinger, M. (2009). Antarctic crustal thickness from satellite gravity: Implications for the transantarctic and gamburtsev subglacial mountains. *Earth and Planetary Science Letters*, *288*(1), 194–203. https://doi.org/10.1016/j.epsl.2009.09.022

Bosch, M., Meza, R., Jiménez, R., & Hönig, A. (2006). Joint gravity and magnetic inversion in 3D using Monte Carlo methods. *Geophysics*, *71*(4), G153–G156. https://doi.org/10.1190/1.2209952

Bozzo, E., Caneva, G., Capponi, G., & Colla, A. (1995). Magnetic investigations of the junction between Wilson and Bowers terranes (northern Victoria Land, Antarctica). *Antarctic Science*, *7*(2), 149–157. https://doi.org/10.1017/S0954102095000216

Bozzo, E., Colla, A., & Meloni, A. (1992). *Ground magnetics in north Victoria Land (East Antarctica)* (pp. 563–569). Recent Progress in Antarctic Earth Science, Terra Scientific Publishing Company.

Burton-Johnson, A., Dziadek, R., & Martin, C. (2020). Review article: Geothermal heat flow in Antarctica: Current and future directions. *The Cryosphere*, *14*(11), 3843–3873. https://doi.org/10.5194/tc-14-3843-2020

Carson, C. J., McLaren, S., Roberts, J. L., Boger, S. D., & Blankenship, D. D. (2014). Hot rocks in a cold place: High sub-glacial heat flow in EastEast Antarctica. *Journal of the Geological Society*, *171*(1), 9–12. https://doi.org/10.1144/jgs2013-030

Cooper, A. F., Maas, R., Scott, J. M., & Barber, A. J. W. (2011). Dating of volcanism and sedimentation in the skelton group, transantarctic mountains: Implications for the Rodinia-Gondwana transition in southern Victoria Land, Antarctica. *GSA Bulletin*, *123*(3–4), 681–702. https://doi.org/10.1130/b30237.1

Cordell, L. (1985). Applications and problems of analytical continuation of New Mexico aeromagnetic data between arbitrary surfaces of very high relief. In *Proceedings of the international meeting on potential fields in rugged topography, Bulletin* (Vol. 7, pp. 96–101). Institute of Geophysics, University of Lausanne.

Cox, S. C., Smith Lyttle, B., Elkind, S., Smith Siddoway, C., Morin, P., Capponi, G., et al. (2023a). A continent-wide detailed geological map dataset of Antarctica. *Scientific Data*, *10*(1), 250. https://doi.org/10.1038/s41597-023-02152-9

Cox, S. C., Smith Lyttle, B., Elkind, S., Smith Siddoway, C., Morin, P., Capponi, G., et al. (2023b). The GeoMAP (v.2022-08) continent-wide detailed geological dataset of Antarctica [Dataset]. *PANGAEA*. https://doi.org/10.1594/PANGAEA.951482

Crameri, F. (2023). Scientific colour maps [Software]. *Zenodo*. https://doi.org/10.5281/zenodo.8035877

DeConto, R. M., & Pollard, D. (2016). Contribution of Antarctica to past and future sea-level rise. *Nature*, *531*(7596), 591–597. https://doi.org/10.1038/nature17145

Direen, N. G., & Crawford, A. J. (2003). Fossil seaward-dipping reflector sequences preserved in southeastern Australia: A 600 Ma volcanic passive margin in eastern Gondwanaland. *Journal of the Geological Society*, *160*(6), 985–990. https://doi.org/10.1144/0016-764903-010

Drewry, D. J. (1976). Sedimentary basins of the east Antarctic craton from geophysical evidence. *Tectonophysics*, *36*(1), 301–314. https://doi.org/10.1016/0040-1951(76)90023-8

Ducea, M. (2001). The California Arc: Thick granitic batholiths, eclogitic residues, lithospheric-scale thrusting, and magmatic flare-ups. *Geological Society of America Today*, *11*, 4. https://doi.org/10.1130/1052-5173(2001)011<0004:Tcatgb>2.0.Co2

Elson, P., Sales De Andrade, E., Lucas, G., May, R., Hattersley, R., Campbell, E., et al. (2022). SciTools/cartopy: V0.21.1 [Software]. *Zenodo*. https://doi.org/10.5281/zenodo.7430317

Estrada, S., Läufer, A., Eckelmann, K., Hofmann, M., Gärtner, A., & Linnemann, U. (2016). Continuous neoproterozoic to ordovician sedimentation at the East Gondwana margin — Implications from detrital zircons of the Ross orogen in northern Victoria Land, Antarctica. *Gondwana Research*, *37*, 426–448. https://doi.org/10.1016/j.gr.2015.10.006

Fahnestock, M., Abdalati, W., Joughin, I., Brozena, J., & Gogineni, P. (2001). High geothermal heat flow, basal melt, and the origin of rapid ice flow in Central Greenland. *Science*, *294*(5550), 2338–2342. https://doi.org/10.1126/science.1065370

Ferraccioli, F., Armadillo, E., Jordan, T. A., Bozzo, E., & Corr, H. (2009). Aeromagnetic exploration over the East Antarctic ice sheet: A new view of the Wilkes Subglacial Basin. *Tectonophysics*, *478*(1), 62–77. https://doi.org/10.1016/j.tecto.2009.03.013

Ferraccioli, F., Armadillo, E., Zunino, A., Bozzo, E., Rocchi, S., & Armienti, P. (2009). Magmatic and tectonic patterns over the Northern Victoria Land sector of the Transantarctic Mountains from new aeromagnetic imaging. *Tectonophysics*, *478*(1), 43–61. https://doi.org/10.1016/j.tecto.2008.11.028

Ferraccioli, F., & Bozzo, E. (2003). Cenozoic strike-slip faulting from the eastern margin of the Wilkes Subglacial Basin to the western margin of the Ross Sea Rift: An aeromagnetic connection. *Geological Society, London, Special Publications*, *210*(1), 109–133. https://doi.org/10.1144/GSL.SP.2003.210.01.07

Ferraccioli, F., Coren, F., Bozzo, E., Zanolla, C., Gandolfi, S., Tabacco, I., & Frezzotti, M. (2001). Rifted(?) crust at the East Antarctic craton margin: Gravity and magnetic interpretation along a traverse across the Wilkes Subglacial Basin region. *Earth and Planetary Science Letters*, *192*(3), 407–421. https://doi.org/10.1016/S0012-821X(01)00459-9

Ferré, E. C., Friedman, S. A., Martín-Hernández, F., Feinberg, J. M., Till, J. L., Ionov, D. A., & Conder, J. A. (2014). Eight good reasons why the uppermost mantle could be magnetic. *Tectonophysics*, *624–625*, 3–14. https://doi.org/10.1016/j.tecto.2014.01.004

Finn, C. A., Moore, D., Damaske, D., & Mackey, T. (1999). Aeromagnetic legacy of early Paleozoic subduction along the Pacific margin of Gondwana. *Geology*, *27*(12), 1087–1090. https://doi.org/10.1130/0091-7613(1999)027<1087:Aloeps>2.3.Co;2

Fisher, A. T., Mankoff, K. D., Tulaczyk, S. M., Tyler, S. W., Foley, N., & Team, a. t. W. S. (2015). High geothermal heat flux measured below the West Antarctic ice sheet. *Science Advances*, *1*(6), e1500093. https://doi.org/10.1126/sciadv.1500093

Fox Maule, C., Purucker, M. E., Olsen, N., & Mosegaard, K. (2005). Heat flux anomalies in Antarctica revealed by satellite magnetic data. *Science*, *309*(5733), 464–467. https://doi.org/10.1126/science.1106888

Franz, G., Moorkamp, M., Jegen, M., Berndt, C., & Rabbel, W. (2021). Comparison of different coupling methods for joint inversion of geophysical data: A case study for the Namibian continental margin. *Journal of Geophysical Research: Solid Earth*, *126*(12), e2021JB022092. https://doi.org/10.1029/2021JB022092

Frederick, B. C., Young, D. A., Blankenship, D. D., Richter, T. G., Kempf, S. D., Ferraccioli, F., & Siegert, M. J. (2016). Distribution of subglacial sediments across the Wilkes Subglacial Basin, East Antarctica. *Journal of Geophysical Research: Earth Surface*, *121*(4), 790–813. https://doi.org/10.1002/2015JF003760

Fregoso, E., & Gallardo, L. A. (2009). Cross-gradients joint 3D inversion with applications to gravity and magnetic data. *Geophysics*, *74*(4), L31–L42. https://doi.org/10.1190/1.3119263

Frey, M., & Ebbing, J. (2020). The deep geothermal potential of the radiogenic Løvstakken Granite in western Norway. *Norwegian Journal of Geology/Norsk Geologisk Forening*, *100*(1). https://doi.org/10.17850/njg100-1-4

Gallardo-Delgado, L. A., Pérez-Flores, M. A., & Gómez-Treviño, E. (2003). A versatile algorithm for joint 3D inversion of gravity and magnetic data. *Geophysics*, *68*(3), 949–959. https://doi.org/10.1190/1.1581067

Gianni, G. M., & Luján, S. P. (2021). Geodynamic controls on magmatic arc migration and quiescence. *Earth-Science Reviews*, *218*, 103676. https://doi.org/10.1016/j.earscirev.2021.103676

Gibson, G. M., Champion, D. C., & Ireland, T. R. (2015). Preservation of a fragmented late Neoproterozoic–earliest Cambrian hyper-extended continental-margin sequence in the Australian Delamerian Orogen. *Geological Society, London, Special Publications*, *413*(1), 269–299. https://doi.org/10.1144/SP413.8

Gillies, S., van der Wel, C., Van den Bossche, J., Taves, M. W., Arnott, J., Ward, B. C., et al. (2022). Shapely [Software]. *Zenodo*. https://doi.org/10.5281/zenodo.7428463

Golynsky, A. V., Ferraccioli, F., Hong, J. K., Golynsky, D. A., von Frese, R. R. B., Young, D. A., et al. (2018a). ADMAP2 Magnetic anomaly map of the Antarctic [Dataset]. *PANGAEA*. https://doi.org/10.1594/PANGAEA.892724

Golynsky, A. V., Ferraccioli, F., Hong, J. K., Golynsky, D. A., von Frese, R. R. B., Young, D. A., et al. (2018b). New magnetic anomaly map of the Antarctic. *Geophysical Research Letters*, *45*(13), 6437–6449. https://doi.org/10.1029/2018GL078153

Goodge, J. W. (2020). Geological and tectonic evolution of the Transantarctic Mountains, from ancient craton to recent enigma. *Gondwana Research*, *80*, 50–122. https://doi.org/10.1016/j.gr.2019.11.001

Goodge, J. W., Fanning, C. M., Fisher, C. M., & Vervoort, J. D. (2024). Crustal architecture of the Paleo-Pacific rift margin of EastEast Antarctica: Evidence from U-Pb ages and O-Hf Isotope compositions of Ross orogen granitoids. *Geochemistry, Geophysics, Geosystems*, *25*(4), e2024GC011435. https://doi.org/10.1029/2024GC011435

Goodge, J. W., Fanning, C. M., Norman, M. D., & Bennett, V. C. (2012). Temporal, isotopic and spatial relations of early paleozoic Gondwana-margin arc magmatism, central Transantarctic mountains, Antarctica. *Journal of Petrology*, *53*(10), 2027–2065. https://doi.org/10.1093/petrology/egs043

Goodge, J. W., & Finn, C. A. (2010). Glimpses of East Antarctica: Aeromagnetic and satellite magnetic view from the central transantarctic mountains of EastEast Antarctica. *Journal of Geophysical Research*, *115*(B9). https://doi.org/10.1029/2009JB006890

Goodge, J. W., Myrow, P., Williams, I. S., & Bowring, S. A. (2002). Age and provenance of the beardmore group, Antarctica: Constraints on Rodinia supercontinent breakup. *The Journal of Geology*, *110*(4), 393–406. https://doi.org/10.1086/340629

Guillen, A., & Menichetti, V. (1984). Gravity and magnetic inversion with minimization of a specific functional. *Geophysics*, *49*(8), 1354–1360. https://doi.org/10.1190/1.1441761

Haber, E., & Holtzman Gazit, M. (2013). Model fusion and joint inversion. *Surveys in Geophysics*, *34*(5), 675–695. https://doi.org/10.1007/s10712-013-9232-4

Haeger, C., Petrunin, A. G., & Kaban, M. K. (2022). Geothermal heat flow and thermal structure of the Antarctic lithosphere. *Geochemistry, Geophysics, Geosystems*, *23*(10), e2022GC010501. https://doi.org/10.1029/2022GC010501

Hansen, S. E., Kenyon, L. M., Graw, J. H., Park, Y., & Nyblade, A. A. (2016). Crustal structure beneath the northern transantarctic mountains and Wilkes Subglacial Basin: Implications for tectonic origins. *Journal of Geophysical Research: Solid Earth*, *121*(2), 812–825. https://doi.org/10.1002/2015JB012325

Harris, C. R., Millman, K. J., van der Walt, S. J., Gommers, R., Virtanen, P., Cournapeau, D., et al. (2020). Array programming with NumPy. *Nature*, *585*(7825), 357–362. https://doi.org/10.1038/s41586-020-2649-2

Hasterok, D., & Chapman, D. S. (2011). Heat production and geotherms for the continental lithosphere. *Earth and Planetary Science Letters*, *307*(1), 59–70. https://doi.org/10.1016/j.epsl.2011.04.034

Hunter, J. (2007). Matplotlib: A 2D graphics environment. *Computing in Science & Engineering*, *9*(3), 90–95. https://doi.org/10.1109/MCSE.2007.55

Johnson, A. C. (1999). Interpretation of new aeromagnetic anomaly data from the central Antarctic Peninsula. *Journal of Geophysical Research*, *104*(B3), 5031–5046. https://doi.org/10.1029/1998JB900073

Jordahl, K., Van den Bossche, J., Wasserman, J., McBride, J., Gerard, J., Tratner, J., et al. (2020). geopandas/geopandas: V0.8.1 [Software]. https://doi.org/10.5281/zenodo.3946761

Jordan, T. A., Ferraccioli, F., Armadillo, E., & Bozzo, E. (2013). Crustal architecture of the Wilkes Subglacial Basin in East Antarctica, as revealed from airborne gravity data. *Tectonophysics*, *585*, 196–206. https://doi.org/10.1016/j.tecto.2012.06.041

Kluyver, T., Ragan-Kelley, B., Pérez, F., Granger, B., Bussonnier, M., Frederic, J., et al. (2016). *Jupyter notebooks—a publishing format for reproducible computational workflows, positioning and power in academic publishing: Players, agents and agendas* (pp. 87–90). IOS Press.

Lamarque, G., Bascou, J., Ménot, R.-P., Paquette, J.-L., Couzinié, S., Rolland, Y., & Cottin, J.-Y. (2018). Ediacaran to lower Cambrian basement in eastern George V Land (Antarctica): Evidence from UPb dating of gneiss xenoliths and implications for the South Australia- East Antarctica connection. *Lithos*, *318–319*, 219–229. https://doi.org/10.1016/j.lithos.2018.08.021

Lanza, R., & Tonarini, S. (1998). Palaeomagnetic and geochronological results from the cambro-ordovician granite Harbour intrusives inland of Terra Nova Bay (Victoria Land, Antarctica). *Geophysical Journal International*, *135*(3), 1019–1027. https://doi.org/10.1046/j.1365-246X.1998.00692.x

Leat, P. T., Jordan, T. A., Flowerdew, M. J., Riley, T. R., Ferraccioli, F., & Whitehouse, M. J. (2018). Jurassic high heat production granites associated with the Weddell Sea rift system, Antarctica. *Tectonophysics*, *722*, 249–264. https://doi.org/10.1016/j.tecto.2017.11.011

Li, L., & Aitken, A. R. A. (2024). Crustal heterogeneity of Antarctica signals spatially variable radiogenic heat production. *Geophysical Research Letters*, *51*(2), e2023GL106201. https://doi.org/10.1029/2023GL106201

Li, Y., Lu, Y., & Siegert, M. J. (2020). Radar sounding confirms a hydrologically active deep-water subglacial lake in EastEast Antarctica. *Frontiers in Earth Science*, *8*. https://doi.org/10.3389/feart.2020.00294

Livingstone, S. J., Li, Y., Rutishauser, A., Sanderson, R. J., Winter, K., Mikucki, J. A., et al. (2022). Subglacial lakes and their changing role in a warming climate. *Nature Reviews Earth & Environment*, *3*(2), 106–124. https://doi.org/10.1038/s43017-021-00246-9

Lösing, M., & Ebbing, J. (2021a). Predicted Antarctic heat flow and uncertainties using machine learning [Dataset]. *PANGAEA*. https://doi.org/10.1594/PANGAEA.930237

Lösing, M., & Ebbing, J. (2021b). Predicting geothermal heat flow in Antarctica with a machine learning approach. *Journal of Geophysical Research: Solid Earth*, *126*(6), e2020JB021499. https://doi.org/10.1029/2020JB021499

Lösing, M., Moorkamp, M., & Ebbing, J. (2022). Joint inversion based on variation of information - a crustal model of Wilkes Land, East Antarctica. *Geophysical Journal International*, *232*(1), 162–175. https://doi.org/10.1093/gji/ggac334

Lowe, M. (2023). VI_inversion_WSB_TAM_JGRse (v1.0) [Software]. *Zenodo*. https://doi.org/10.5281/zenodo.8304212

Lowe, M., Jordan, T., Ebbing, J., Koglin, N., Ruppel, A., Moorkamp, M., et al. (2024). Comparing geophysical inversion and petrophysical measurements for northern Victoria Land, Antarctica. *Geophysical Journal International*, *239*(1), 276–291. https://doi.org/10.1093/gji/ggae272

Lowe, M., Jordan, T., Moorkamp, M., Ebbing, J., Green, C., Lösing, M., & Larter, R. (2023). 3D density and susceptibility distribution of the Wilkes Subglacial Basin and transantarctic mountains in East Antarctica, (version 1.0) [Dataset]. *NERC EDS UK Polar Data Centre*. https://doi.org/10.5285/5e1424e7-124d-4cc3-ba06-b2285c0b458c

Lowe, M., Mather, B., Green, C., Jordan, T. A., Ebbing, J., & Larter, R. (2022). Curie depth points and Geothermal heat flow estimates from spectral analysis of magnetic data in the Transantarctic Mountains and Wilkes Subglacial Basin region, (Version 1.0) [Dataset]. *NERC EDS UK Polar Data Centre*. https://doi.org/10.5285/B8DCBAA9-3AC0-42BD-95A5-6B5961CBCB7E

Lowe, M., Mather, B., Green, C., Jordan, T. A., Ebbing, J., & Larter, R. (2023). Anomalously high heat flow regions beneath the transantarctic mountains and Wilkes Subglacial Basin in EastEast Antarctica inferred from Curie depth. *Journal of Geophysical Research: Solid Earth*, *128*(1), e2022JB025423. https://doi.org/10.1029/2022JB025423

Mandolesi, E., & Jones, A. G. (2014). Magnetotelluric inversion based on mutual information. *Geophysical Journal International*, *199*(1), 242–252. https://doi.org/10.1093/gji/ggu258

Martos, Y. M., Catalán, M., Jordan, T. A., Golynsky, A., Golynsky, D., Eagles, G., & Vaughan, D. G. (2017a). Antarctic geothermal heat flux distribution and estimated Curie Depths, links to gridded files [Dataset]. *PANGAEA*. https://doi.org/10.1594/PANGAEA.882503

Martos, Y. M., Catalán, M., Jordan, T. A., Golynsky, A., Golynsky, D., Eagles, G., & Vaughan, D. G. (2017b). Heat flux distribution of Antarctica unveiled. *Geophysical Research Letters*, *44*(22), 11417–11426. https://doi.org/10.1002/2017GL075609

Maslanyj, M. P., Garrett, S. W., Johnson, A. C., Renner, A. C., & Smith, A. M. (1991). *Aeromagnetic anomaly map of west Antarctica (Weddell Sea sector), scale 1:2,500,000, BAS GEOMAP series, sheet 2, 20-22*. British Antarctic Survey.

McKinney, W. (2010). Data structures for statistical computing in python. *Proceedings of the 9th Python in Science Conference*, *445*(1), 51–56.

McMillan, M., Corr, H., Shepherd, A., Ridout, A., Laxon, S., & Cullen, R. (2013). Three-dimensional mapping by CryoSat-2 of subglacial lake volume changes. *Geophysical Research Letters*, *40*(16), 4321–4327. https://doi.org/10.1002/grl.50689

Moorkamp, M. (2021). Joint inversion of gravity and magnetotelluric data from the Ernest-Henry IOCG deposit with a variation of information constraint. In *First international meeting for applied geoscience & energy expanded abstracts*. (pp. 1711–1715). Society of Exploration Geophysicists. https://doi.org/10.1190/segam2021-3582000.1

Moorkamp, M. (2022). Deciphering the state of the lower crust and upper mantle with multi-physics inversion. *Geophysical Research Letters*, *49*(9), e2021GL096336. https://doi.org/10.1029/2021GL096336

Moorkamp, M., Heincke, B., Jegen, M., Roberts, A. W., & Hobbs, R. W. (2011). A framework for 3-D joint inversion of MT, gravity and seismic refraction data. *Geophysical Journal International*, *184*(1), 477–493. https://doi.org/10.1111/j.1365-246X.2010.04856.x

Moorkamp, M., Heincke, B., Shi, Z., & Weise, B. (2023). Joint inversion framework in three dimensions (JIF3D) [Software]. https://sourceforge.net/projects/jif3d/edited

Morelli, A., & Danesi, S. (2004). Seismological imaging of the Antarctic continental lithosphere: A review. *Global and Planetary Change*, *42*(1), 155–165. https://doi.org/10.1016/j.gloplacha.2003.12.005

Morlighem, M., Rignot, E., Binder, T., Blanenship, D., Drews, R., Eagles, G., et al. (2022). MEaSUREs BedMachine Antarctica, version 3 [Dataset]. *NASA National Snow and Ice Data Center Distributed Active Archive Center*. https://doi.org/10.5067/FPSU0V1MWUB6

Morlighem, M., Rignot, E., Binder, T., Blankenship, D., Drews, R., Eagles, G., et al. (2020). Deep glacial troughs and stabilizing ridges unveiled beneath the margins of the Antarctic ice sheet. *Nature Geoscience*, *13*(2), 132–137. https://doi.org/10.1038/s41561-019-0510-8

Murphy, B., Yurchak, R., & Müller, S. (2022). GeoStat-framework/PyKrige: V1.7.0 [Software]. *Zenodo*. https://doi.org/10.5281/zenodo.7008206

Ohneiser, C., Wilson, G. S., & Cox, S. C. (2015). Characterisation of magnetic minerals from southern Victoria Land, Antarctica. *New Zealand Journal of Geology and Geophysics*, *58*(1), 52–65. https://doi.org/10.1080/00288306.2014.990044

Pappa, F., Ebbing, J., & Ferraccioli, F. (2019). Moho depths of Antarctica: Comparison of seismic, gravity, and isostatic results. *Geochemistry, Geophysics, Geosystems*, *20*(3), 1629–1645. https://doi.org/10.1029/2018GC008111

Pappa, F., Ebbing, J., Ferraccioli, F., & van der Wal, W. (2019). Modeling satellite gravity gradient data to derive density, temperature, and viscosity structure of the Antarctic lithosphere. *Journal of Geophysical Research: Solid Earth*, *124*(11), 12053–12076. https://doi.org/10.1029/2019JB017997

Paulsen, T., Encarnación, J., Grunow, A., Benowitz, J., Layer, P., Deering, C., & Sliwinski, J. (2023). Outboard onset of Ross orogen magmatism and subsequent igneous and metamorphic cooling linked to slab rollback during late-stage Gondwana assembly. *Geosciences*, *13*(4), 126. https://doi.org/10.3390/geosciences13040126

Paxman, G. J. G., Jamieson, S. S. R., Ferraccioli, F., Bentley, M. J., Ross, N., Armadillo, E., et al. (2018). Bedrock erosion surfaces record former East Antarctic ice sheet extent. *Geophysical Research Letters*, *45*(9), 4114–4123. https://doi.org/10.1029/2018GL077268

Paxman, G. J. G., Jamieson, S. S. R., Ferraccioli, F., Bentley, M. J., Ross, N., Watts, A. B., et al. (2019). The role of lithospheric flexure in the landscape evolution of the Wilkes Subglacial Basin and transantarctic mountains, East Antarctica. *Journal of Geophysical Research: Earth Surface*, *124*(3), 812–829. https://doi.org/10.1029/2018JF004705

Pollard, D., DeConto, R. M., & Alley, R. B. (2015). Potential Antarctic Ice Sheet retreat driven by hydrofracturing and ice cliff failure. *Earth and Planetary Science Letters*, *412*, 112–121. https://doi.org/10.1016/j.epsl.2014.12.035

Reading, A. M., Stål, T., Halpin, J. A., Lösing, M., Ebbing, J., Shen, W., et al. (2022). Antarctic geothermal heat flow and its implications for tectonics and ice sheets. *Nature Reviews Earth & Environment*, *3*(12), 814–831. https://doi.org/10.1038/s43017-022-00348-y

Reitmayr, G., Korth, W., Caneva, G., & Ferraccioli, F. (2003). Gravity survey at the oates coast area, East Antarctica, during the joint German-Italian expedition 1999/2000. *Terra Antartica*, *10*, 97–104.

Robinson, E. S., & Splettstoesser, J. F. (1986). Structure of the transantarctic mountains determined from geophysical surveys. *Geology of the Central Transantarctic Mountains*, *36*, 119–162. https://doi.org/10.1029/AR036p0119

Saleeby, J., Ducea, M., & Clemens-Knott, D. (2003). Production and loss of high-density batholithic root, southern Sierra Nevada, California. *Tectonics*, *22*(6). https://doi.org/10.1029/2002TC001374

Scheinert, M., Ferraccioli, F., Schwabe, J., Bell, R., Studinger, M., Damaske, D., et al. (2016a). Antarctic free-air and complete Bouguer gravity anomaly grid [Dataset]. *PANGAEA*. https://doi.pangaea.de/10.1594/PANGAEA.848168

Scheinert, M., Ferraccioli, F., Schwabe, J., Bell, R., Studinger, M., Damaske, D., et al. (2016b). New Antarctic gravity anomaly grid for enhanced geodetic and geophysical studies in Antarctica. *Geophysical Research Letters*, *43*(2), 600–610. https://doi.org/10.1002/2015GL067439

Schoof, C. (2007). Ice sheet grounding line dynamics: Steady states, stability, and hysteresis. *Journal of Geophysical Research*, *112*(F3). https://doi.org/10.1029/2006JF000664

Shamsipour, P., Marcotte, D., & Chouteau, M. (2012). 3D stochastic joint inversion of gravity and magnetic data. *Journal of Applied Geophysics*, *79*, 27–37. https://doi.org/10.1016/j.jappgeo.2011.12.012

Shen, W., Wiens, D. A., Lloyd, A. J., & Nyblade, A. A. (2020). A geothermal heat flux map of Antarctica empirically constrained by seismic structure. *Geophysical Research Letters*, *47*(14), e2020GL086955. https://doi.org/10.1029/2020GL086955

Siegert, M. J., & Dowdeswell, J. A. (1996). Spatial variations in heat at the base of the Antarctic ice sheet from analysis of the thermal regime above subglacial lakes. *Journal of Glaciology*, *42*(142), 501–509. https://doi.org/10.3189/S0022143000003488

Smith, B. E., Fricker, H. A., Joughin, I. R., & Tulaczyk, S. (2009). An inventory of active subglacial lakes in Antarctica detected by ICESat (2003–2008). *Journal of Glaciology*, *55*(192), 573–595. https://doi.org/10.3189/002214309789470879

Smith, W. H. F., & Wessel, P. (1990). Gridding with continuous curvature splines in tension. *Geophysics*, *55*(3), 293–305. https://doi.org/10.1190/1.1442837

Stål, T., Halpin, J. A., Goodge, J. W., & Reading, A. M. (2024). Geology matters for Antarctic geothermal heat. *Geophysical Research Letters*, *51*(13), e2024GL110098. https://doi.org/10.1029/2024GL110098

Stål, T., Reading, A. M., Halpin, J. A., & Whittaker, J. (2020). Antarctic geothermal heat flow model: Aq1 [Dataset]. *PANGAEA*. https://doi.org/10.1594/PANGAEA.924857

Stål, T., Reading, A. M., Halpin, J. A., & Whittaker, J. M. (2021). Antarctic geothermal heat flow model: Aq1. *Geochemistry, Geophysics, Geosystems*, *22*(2), e2020GC009428. https://doi.org/10.1029/2020GC009428

Steed, R. N. (1983). Structural interpretations of Wilkes Land, Antarctica. *Antarctic earth science. International symposium*, *4*.

Stern, T. A., & ten Brink, U. S. (1989). Flexural uplift of the transantarctic mountains. *Journal of Geophysical Research*, *94*(B8), 10315–10330. https://doi.org/10.1029/JB094iB08p10315

Stokes, C. R., Abram, N. J., Bentley, M. J., Edwards, T. L., England, M. H., Foppert, A., et al. (2022). Response of the East Antarctic ice sheet to past and future climate change. *Nature*, *608*(7922), 275–286. https://doi.org/10.1038/s41586-022-04946-0

Studinger, M., Bell, R. E., Buck, W. R., Karner, G. D., & Blankenship, D. D. (2004). Sub-ice geology inland of the Transantarctic Mountains in light of new aerogeophysical data. *Earth and Planetary Science Letters*, *220*(3), 391–408. https://doi.org/10.1016/S0012-821X(04)00066-4

Subrahmanyam, C., & Verma, R. (1981). Densities and magnetic susceptibilities of precambrian rocks of different metamorphic grade (southern indian shield). *Journal of Geophysics*, *49*(1), 101–107. Retrieved from https://journal.geophysicsjournal.com/JofG/article/view/251

ten Brink, U. S., Hackney, R. I., Bannister, S., Stern, T. A., & Makovsky, Y. (1997). Uplift of the transantarctic mountains and the bedrock beneath the East Antarctic ice sheet. *Journal of Geophysical Research*, *102*(B12), 27603–27621. https://doi.org/10.1029/97JB02483

ten Brink, U. S., & Stern, T. (1992). Rift flank uplifts and hinterland basins: Comparison of the transantarctic mountains with the great escarpment of southern Africa. *Journal of Geophysical Research*, *97*(B1), 569–585. https://doi.org/10.1029/91JB02231

Virtanen, P., Gommers, R., Oliphant, T. E., Haberland, M., Reddy, T., Cournapeau, D., et al. (2020). SciPy 1.0: Fundamental algorithms for scientific computing in Python. *Nature Methods*, *17*(3), 261–272. https://doi.org/10.1038/s41592-019-0686-2

Zanutta, A., Negusini, M., Vittuari, L., Martelli, L., Cianfarra, P., Salvini, F., et al. (2018). New geodetic and gravimetric maps to infer geodynamics of Antarctica with insights on Victoria Land. *Remote Sensing*, *10*(10), 1608. https://doi.org/10.3390/rs10101608